

SPATIAL CORRELATION FUNCTION OF X-RAY SELECTED AGN

C.R. MULLIS¹, J.P. HENRY², I.M. GIOIA³, H. BÖHRINGER⁴,
U.G. BRIEL⁴, W. VOGES⁴, AND J.P. HUCHRA⁵

ABSTRACT

We present a detailed description of the first direct measurement of the spatial correlation function of X-ray selected AGN. This result is based on an X-ray flux-limited sample of 219 AGN discovered in the contiguous 80.7 deg² region of the *ROSAT* North Ecliptic Pole (NEP) Survey. Clustering is detected at the 4 σ level at comoving scales in the interval $r = 5 - 60 h^{-1}$ Mpc. Fitting the data with a power law of slope $\gamma = 1.8$, we find a correlation length of $r_0 = 7.4^{+1.8}_{-1.9} h^{-1}$ Mpc ($\Omega_M = 0.3$, $\Omega_\Lambda = 0.7$). The median redshift of the AGN contributing to the signal is $z_\xi = 0.22$. This clustering amplitude implies that X-ray selected AGN are spatially distributed in a manner similar to that of optically selected AGN. Furthermore, the *ROSAT* NEP determination establishes the local behavior of AGN clustering, a regime which is poorly sampled in general. Combined with high-redshift measures from optical studies, the *ROSAT* NEP results argue that the AGN correlation strength essentially does not evolve with redshift, at least out to $z \sim 2.2$. In the local Universe, X-ray selected AGN appear to be unbiased relative to galaxies and the inferred X-ray bias parameter is near unity, $b_X \sim 1$. Hence X-ray selected AGN closely trace the underlying mass distribution. The *ROSAT* NEP AGN catalog, presented here, features complete optical identifications and spectroscopic redshifts. The median redshift, X-ray flux, and X-ray luminosity are $z = 0.41$, $f_X = 1.1 \times 10^{-13}$ ergs cm⁻² s⁻¹, and $L_X = 9.2 \times 10^{43} h_{70}^{-2}$ ergs s⁻¹ (0.5–2.0 keV), respectively. Unobscured, type 1 AGN are the dominant constituents (90%) of this soft X-ray selected sample of AGN.

Subject headings: quasars: general — cosmology: observations — large-scale structure of universe — X-rays: general

1. INTRODUCTION

Active galactic nuclei (AGN) are presumably the very luminous manifestations of accretion onto supermassive black holes. Shining brightly across the electromagnetic spectrum and easily detectable to very high redshift, AGN are accessible tracers of galaxy formation and evolution as well as large-scale structure. The spatial distribution of AGN reflects the distribution of matter fluctuations modulated by the complex, non-linear astrophysics of black hole formation. Thus measurements of AGN clustering and its evolution provide important tests for models of AGN formation in an adopted cosmological reference frame (Hartwick & Schade 1990).

The vast majority of work on this topic has focused on optical surveys for quasi-stellar objects (QSOs). Following the first attempt to measure AGN clustering by Osmer (1981), the first significant detection came from the work of Shaver (1984). In the ensuing years sample sizes have increased as has the resulting precision (Shanks et al. 1987; Iovino & Shaver 1988; Andreani & Cristiani 1992; Mo & Fang 1993; Shanks & Boyle 1994; Croom & Shanks 1996; La Franca et al. 1998). There is broad agreement

in the conclusions of these studies. Clustering is detected at the ~ 3 – 4σ level. The spatial distribution is characterized using the conventional approach of the two-point correlation function which tracks the excess probability over random to find two objects separated by a given distance. This function is found to have a power-law shape with a slope of $\gamma \approx 1.8$. The clustering scale length, where the correlation function is unity, is $r_0 \sim 6 h^{-1}$ Mpc measured at a mean redshift of $\bar{z} \sim 1.4$. This amplitude is comparable to that found for luminous, local galaxies, and larger than that of dwarf or low surface brightness galaxies (e.g., the results from the Sloan Digital Sky Survey: Zehavi et al. 2002 and the 2dF Galaxy Redshift Survey: Hawkins et al. 2003). This is consistent with the idea that moderately powerful AGN are found in moderately luminous galaxies, and so share their clustering properties.

One question left unresolved by the aforementioned papers is the nature of the clustering evolution, the redshift-dependent behavior of the scale length. Croom et al. (2001) have used the 2dF QSO Redshift Survey (2QZ) to definitively redress this issue, at least in the high redshift interval, and have found essentially no change in the clustering amplitude between $z \sim 0.5$ and $z \sim 2.2$ (see also Croom et al. 2003). The recent measure by Grazian et al. (2004) of the local AGN population lends further support to this largely flat behavior.

At X-ray wavelengths there are far fewer results on the clustering of AGN chiefly due to a historic lack of sufficiently large X-ray samples, particularly those with comprehensive optical follow-up. The *ROSAT* all-sky survey (1990–1991), the first with an imaging X-ray detector, and the subsequent program of pointed observations en-

¹ European Southern Observatory, Headquarters, Karl-Schwarzschild-Strasse 2, Garching bei München D-85748, Germany, cmullis@eso.org

² Institute for Astronomy, University of Hawai'i, 2680 Woodlawn Drive, Honolulu, HI 96822

³ Istituto di Radioastronomia del CNR, via Gobetti 101, Bologna, I-40129, Italy

⁴ Max-Planck Institut für extraterrestrische Physik, Giessenbachstrasse 1603, Garching, D-85741, Germany

⁵ Harvard-Smithsonian Center for Astrophysics, 60 Garden Street, Cambridge, MA 02138

abled the first significant steps forward. Despite the currently limited development, this field is anticipated to experience rapid growth with the advent of much deeper surveys from *Chandra*, *XMM-Newton* and future X-ray survey missions.

The use of X-rays in the selection and characterization of AGN is a natural choice. X-ray emission appears to be a universal feature of AGN (Elvis et al. 1978), and essentially all optically selected AGN are X-ray luminous (Avni & Tananbaum 1986). In fact, X-ray emission is likely the least biased selection technique, particularly at hard energies above 2 keV (Mushotzky 2004).

There have been several determinations of the angular correlation of X-ray AGN (Vikhlinin & Forman 1995; Akylas et al. 2000; Giacconi et al. 2001; Basilakos et al. 2004). However, translating these results to constraints on the three-dimensional clustering strength requires a number of assumptions that results in only weak constraints on r_0 . Actually measuring the spatial correlation function is more involved since optical identifications and redshift measures are required. Early attempts by Boyle & Mo (1993) and Carrera et al. (1998) using data from *Einstein* and *ROSAT*, respectively, did not yield significant clustering signals.

The first direct measure of the spatial correlation function of X-ray selected AGN was achieved in the context of the *ROSAT* North Ecliptic Pole (NEP) Survey. This result was initially reported by Mullis (2001). In the current paper we provide a detailed description of this clustering analysis. Note that only very recently have additional measures of this kind become available as reported for the *Chandra* deep fields by Gilli et al. (2004).

We describe the *ROSAT* NEP Survey in §2 focusing on the basic properties of the X-ray flux-limited AGN sample and the survey selection function. In §3 the formalism of the clustering analysis is laid out, including a description of the spatial correlation estimator and the Monte Carlo simulations of the survey volume. We present the spatial correlation function of X-ray selected AGN in §4. These results are compared to similar studies at both X-ray and optical wavelengths with emphasis on the evolution of clustering strength with redshift in §5. We close with a summary of the key results in §6.

Unless otherwise stated, we use a cosmological model with the parameters, $H_0 = 70 h_{70} \text{ km s}^{-1} \text{ Mpc}^{-1}$, $\Omega_M = 0.3$, and $\Omega_\Lambda = 0.7$, and refer to this as Λ CDM. However, for the correlation length we use $H_0 = 100 \text{ h}^{-1} \text{ km s}^{-1} \text{ Mpc}^{-1}$ for ready comparison to previous results. Unabsorbed X-ray fluxes and restframe X-ray luminosities are quoted in the 0.5–2.0 keV energy band, unless otherwise indicated. Measurement errors are given at the 68% confidence interval (1σ).

2. THE ROSAT NEP AGN SAMPLE

In the *ROSAT* All-Sky Survey (RASS), an 80.7 deg² region around the NEP ($\alpha_{2000} = 18^{\text{h}}00^{\text{m}}$, $\delta_{2000} = +66^{\circ}33'$) constitutes one of the deepest observations of the X-ray sky ever achieved with such a large, contiguous solid angle (Mullis 2001; Henry et al. 2001; Voges et al. 2001). Here 445 unique X-ray sources are detected with fluxes measured at greater than 4σ significance in the 0.5–2.0 keV energy band. The median and maximum exposure times are approximately 5 and 38 ks, respectively. We have identified the physical

nature of 443 (99.6%) of the *ROSAT* NEP X-ray sources through a comprehensive program of imaging and spectroscopy (Gioia et al. 2003). AGN are the dominant constituents comprising nearly half (49.4%) of identified sources in the *ROSAT* NEP Survey catalog (Figure 1).

The *ROSAT* NEP AGN are particularly well suited for a clustering analysis. The AGN are drawn from a contiguous, wide-angle region in the sky sampled to a relatively deep X-ray flux. The survey selection function is well determined and is only a function of X-ray flux. We have identified all but two of the 445 X-ray sources in the survey region. Thus the AGN sample is essentially complete and requires no complicated assumptions to correct for incompleteness. Furthermore, we have spectroscopically measured redshifts for the entire sample.

2.1. Basic Properties

We present the full sample of 219 *ROSAT* NEP AGN in Table 1. This includes several notable revisions relative to previous versions of the catalog (Mullis 2001; Gioia et al. 2003). First, the AGN fluxes and luminosities previously reported were over-estimated by approximately 20% on average due to an error in the conversion of X-ray count rate to flux.⁶ Second, the sample has grown by one due to the re-classification of an X-ray source (RX J1824.7+6509; see footnote in Table 1). And finally, we have adopted the presently-favored “concordance” cosmology in computing X-ray luminosities. The revised and updated catalog with corrected properties is presented in this paper and should be the reference point in any future work with the *ROSAT* NEP AGN sample. Below we explain the columns of Table 1.

Columns (1) and (2): the object name and internal identification number. Sources are listed in order of increasing right ascension.

Columns (3) and (4): the right ascension and declination of the X-ray centroid, respectively.

Columns (5) and (6): the right ascension and declination of the optical counterpart, respectively.

Column(7): Column density of Galactic hydrogen from Elvis et al. (1994) with supplements from Stark et al. (1992).

Columns (8) and (9): Count rate and count rate error in the 0.1–2.4 keV energy band measured within a circular aperture of 5' radius. The quoted error is the 1σ uncertainty based on a maximum-likelihood analysis.

Column (10): Unabsorbed flux in the 0.5–2.0 keV energy band derived from the count rate assuming the source has a power-law spectrum (photon index $\Gamma = 2$), with absorption fixed at the Galactic value for the source position. This total flux includes a correction factor of 1.0369 which accounts for the small fraction of point source flux falling outside the photometry aperture.

Column (11): Rest-frame, K-corrected luminosity in the 0.5–2.0 keV energy band. Note the K-correction for a power-law spectrum is $(1+z)^{\Gamma-2}$ and is thus unity for $\Gamma = 2$ (cosmology: $H_0 = 70 h_{70} \text{ km s}^{-1} \text{ Mpc}^{-1}$, $\Omega_M = 0.3$, and $\Omega_\Lambda = 0.7$).

⁶ A power-law photon index of $\Gamma=1$ was mistakenly used instead of $\Gamma=2$ due to a typographical error in the analysis software. X-ray fluxes and luminosities for galaxy clusters and stars in the referenced works are not affected by this problem.

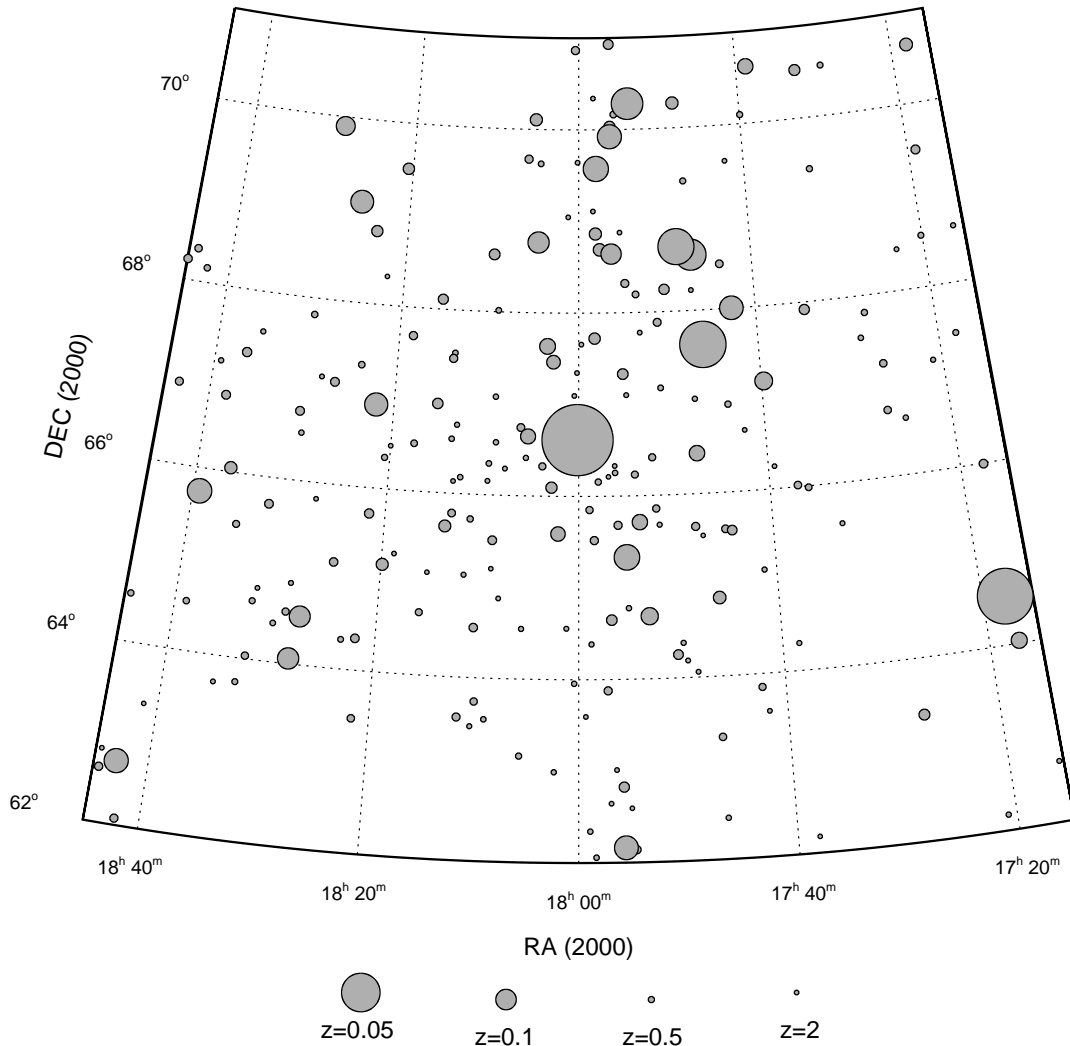


FIG. 1.— Distribution on the sky of the 219 AGN in the *ROSAT* NEP Survey (Aitoff projection). To give some perception of the three-dimensional arrangement of the sample, the symbol size reflects the projected size of a constant physical radius of $500 h^{-1}$ kpc at the redshift of the AGN. As the X-ray emitting region of AGN is sub-parsec, this scale is greatly exaggerated for visualization purposes. An animated “fly-through” of the *ROSAT* NEP Survey volume is available at <http://www.ifa.hawaii.edu/~mullis/nep3d.html>.

Column (12): Spectroscopic redshift (typical uncertainty < 0.001).

Column (13): AGN classification based on the equivalent width of emission lines and the broadness of permitted lines (1 = type 1, 2 = type 2).

We have secured spectroscopic redshifts for the entire *ROSAT* NEP AGN sample; the full range is $z = 0.026 - 3.89$ and the median is $z = 0.41$. X-ray luminosities range over $10^{41} - 10^{46}$ ergs s^{-1} with a median

of $L_X = 9.2 \times 10^{43} h_{70}^{-2}$ ergs s^{-1} . Since *ROSAT* has very limited sensitivity to hard X-rays above 2 keV, the bulk of the NEP AGN (90.4%, 198 objects) are type I AGN (QSOs and Seyfert 1 galaxies) based on the equivalent width and the broadness of their permitted emission lines ($W_\lambda \geq 5 \text{ \AA}$, $\text{FWHM} \geq 2000 \text{ km s}^{-1}$). The remaining 21 NEP AGN (9.6%) are categorized as type II (Seyfert 2 and star-forming galaxies).

2.2. Sky Coverage and $\log N(>S)$ - $\log S$ Distribution

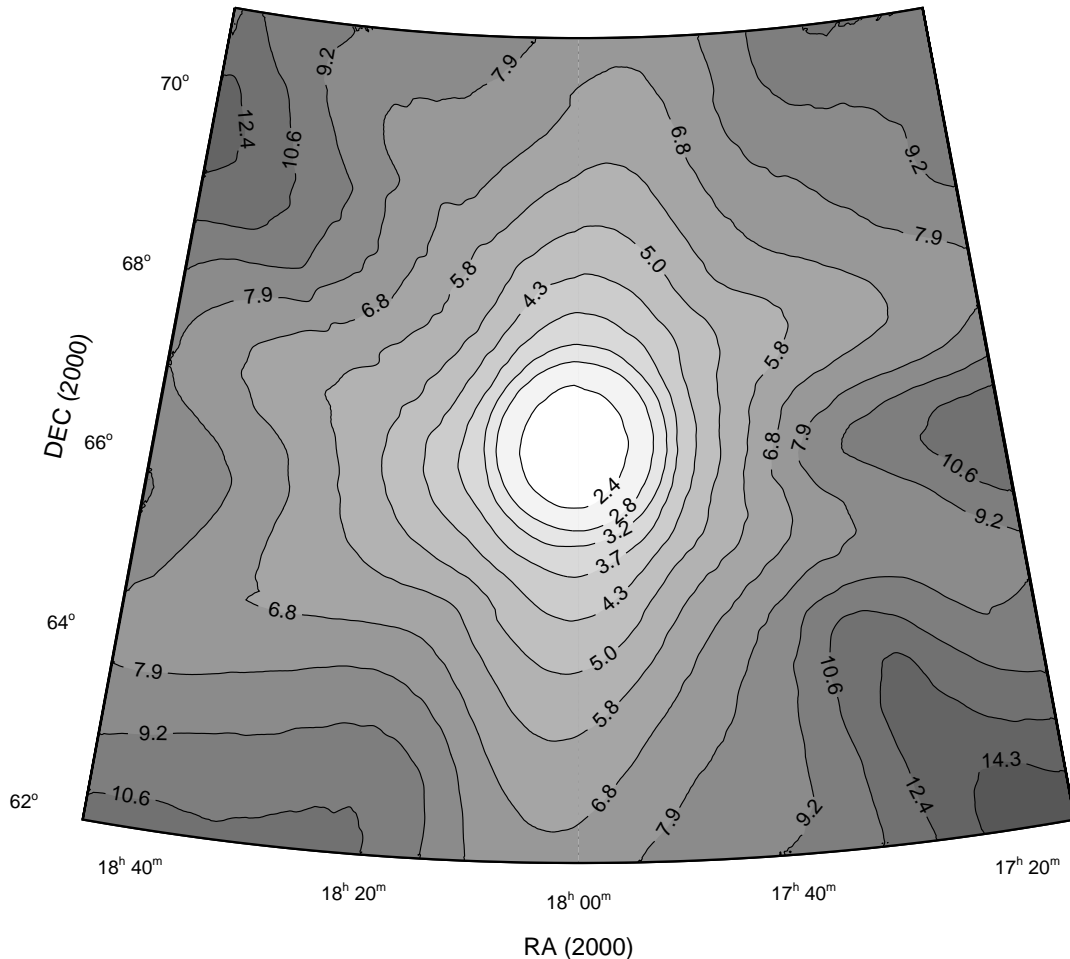


FIG. 2.— Map of the X-ray flux limits for the detection of AGN in the *ROSAT* NEP Survey (Aitoff projection). The logarithmically-spaced contours indicate the minimum total flux that an object must have to meet the 4σ detection requirement of the survey. Contours are labeled in units of 10^{-14} ergs cm^{-2} s^{-1} in the 0.5–2.0 keV energy band. The enhanced sensitivity toward the center of the survey region is a result of the *ROSAT* scan pattern that converges at the NEP.

The distribution on the sky of the 219 *ROSAT* NEP AGN is shown in Figure 1. The average AGN source density is 2.7 deg^{-2} and increases toward the NEP at the center of the survey region as a result of the RASS scan pattern. During the survey phase of the mission, *ROSAT* scanned the sky in great circles which overlapped at the ecliptic poles. The resulting peak in integrated exposure time at the NEP is reflected in the sensitivity map shown in Figure 2. This map of limiting X-ray flux is derived from RASS exposure and background maps (see Chapter 3 of Mullis 2001 and J. P. Henry et al. 2004, in preparation). Here the contours, in units of 10^{-14} ergs cm^{-2} s^{-1} , indicate the minimum flux that an AGN must have to produce at least a 4σ detection and thus meet the selection criterion of the *ROSAT* NEP survey. The sensitivity map is integrated to obtain the final selection function shown in Figure 3. The effective sky coverage is 81 deg^2 at bright fluxes, starts to decrease below 1.3×10^{-13} ergs cm^{-2} s^{-1} , and remains significant down to $\sim 2.3 \times 10^{-14}$ ergs cm^{-2} s^{-1} where the coverage is 1 deg^2 .

In subsequent modeling of the AGN population we will make use of the integral number counts or $\log N(> S) - \log S$ distribution of the *ROSAT* NEP AGN sample. We calculate the number of objects per square degree observed above a flux S by summing up the contribution of each source, weighted by the area in which the source could have been detected, via the equation,

$$N(> S) = \sum_{S_i > S} \frac{1}{\Omega(S_i)}, \quad (1)$$

where S_i is the flux of the i th source and $\Omega(S_i)$ is the sky coverage at flux S_i from Figure 3. A maximum likelihood fit of a power law (Murdoch, Crawford, & Jauncey 1973) to the differential source counts over the flux range $(2\text{--}1000) \times 10^{-14}$ ergs cm^{-2} s^{-1} gives the relation

$$N(> S) = (1.5 \pm 0.1) \left(\frac{S}{10^{-13}} \right)^{-1.30 \pm 0.08} \text{ deg}^{-2}. \quad (2)$$

The normalization is set by the total number of AGN

observed above the minimum survey flux. The measured $\log N(> S) - \log S$ and the power-law fit are plotted in Figure 4. These results are consistent with previous determinations in this flux regime. For example, Hasinger et al. (1993) found a slope of 1.72 ± 0.27 at fluxes $\gtrsim 2.7 \times 10^{-14}$ ergs cm^{-2} s^{-1} , and Mason et al. (2000) report a slope of 1.6 ± 0.3 at fluxes above 3×10^{-14} ergs cm^{-2} s^{-1} .

3. CLUSTERING ANALYSIS

One of the simplest and most popular techniques for characterizing the clustering of objects is the two-point spatial correlation function (Peebles 1980). This statistic is defined in terms of the joint probability (dP) of simultaneously finding an object in a volume dV_1 and another object in a volume dV_2 separated by a distance r ,

$$dP = n^2 [1 + \xi(r)] dV_1 dV_2, \quad (3)$$

where n is the average number density of objects and $\xi(r)$ is the two-point spatial correlation function. In a uniform random Poisson point process, objects are distributed in a completely random pattern and the probabilities of finding objects in dV_1 and dV_2 are independent such that $\xi(r) = 0$. If objects are more clustered than average $\xi(r) > 0$, whereas, if objects are more dispersed than average $\xi(r) < 0$. Hence, the two-point correlation is the excess probability over random to find two objects separated by distance r .

The observed correlation function for a variety of extragalactic objects (e.g., galaxies, AGN, and galaxy clusters) is well fit by a power law of the form

$$\xi(r) = \left(\frac{r}{r_0}\right)^{-\gamma} \quad (4)$$

where the slope is typically $\gamma \approx 1.8$ while the correlation length r_0 depends on the type of object.

3.1. Correlation Estimator

The correlation function is extracted from spatial data via a pairwise analysis. In essence, the number of object pairs of a given spatial separation in the data are compared to the number of object pairs of the same separation from a random catalog. The random catalog is created by homogeneously populating the survey volume in a manner that is consistent with the selection function and boundary conditions of the survey. Hence, an enhancement of the number of data-data pairs relative to the corresponding random-random pairs is indicative of structure in the data.

Though the correlation function can be computed using the natural form, $\xi_n(r) = (DD/RR) - 1$, Landy & Szalay (1993) have demonstrated that the variance is minimized using the estimator,

$$\xi(r) = \frac{N_r(N_r - 1)}{N_d(N_d - 1)} \frac{DD(r)}{RR(r)} - \frac{(N_r - 1)}{N_d} \frac{DR(r)}{RR(r)} + 1. \quad (5)$$

Here $DD(r)$ is the number of data-data pairs in the NEP AGN sample with separations of $r \pm \Delta r/2$ in redshift space. Similarly, $RR(r)$ is the number of random-random pairs and $DR(r)$ is the number of data-random cross-pairs, each with separations of $r \pm \Delta r/2$. The number

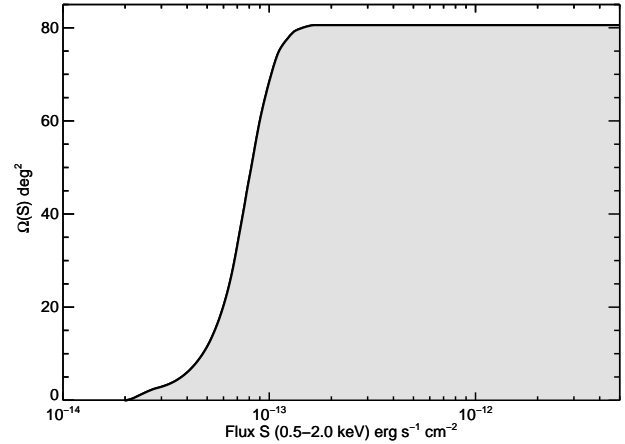


FIG. 3.— Sky coverage for AGN in the *ROSAT* NEP Survey. This is the total area of the sky surveyed as a function of total flux.

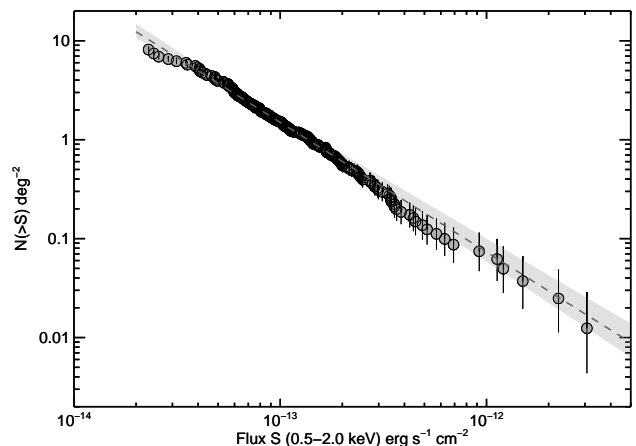


FIG. 4.— Integral number counts per square degree of AGN in the *ROSAT* NEP Survey. The dashed line is a power-law fit to the data derived from a maximum likelihood treatment of the differential number counts. The shaded region is the 1σ error region for this fit.

of objects in the data sample is N_d , and the number of objects in the random sample is N_r . A number of different correlation estimators are commonly used (e.g., Davis & Peebles 1983; Hewett 1982; Hamilton 1993), but a detailed comparison by Kerscher, Szapudi, & Szalay (2000) shows that the Landy & Szalay estimator is preferred in terms of minimal bias and variance, and gives the most reliable results on all spatial scales.

We calculate co-moving separations r between objects in redshift space using the standard relations (e.g., Weinberg 1972; Peebles 1993; Hogg 1999). The transverse co-moving distance between the observer and an object at redshift z is

$$D_M(z) = \frac{c}{H_0 \sqrt{|\Omega_k|}} \times \mathcal{S} \left(\sqrt{|\Omega_k|} \int_0^z dz' [\Omega_M (1+z')^3 + \Omega_k (1+z')^2 + \Omega_\Lambda]^{-1/2} \right) \quad (6)$$

where Ω_M is the matter density parameter, and Ω_Λ is the cosmological constant. The curvature of space is characterized by $\Omega_k = 1 - \Omega_M - \Omega_\Lambda$. The function \mathcal{S} is defined according to:

$$\mathcal{S}(x) \equiv \begin{cases} \sinh x & : \Omega_k > 0 \text{ open universe} \\ x & : \Omega_k = 0 \text{ flat universe} \\ \sin x & : \Omega_k < 0 \text{ closed universe} \end{cases}$$

Note that the transverse co-moving distance (D_M) is related to the luminosity distance (D_L) and the angular diameter distance (D_A) via the equations $D_L = (1+z)D_M$ and $D_A = D_M/(1+z)$.

Consider two objects separated on the sky by an angle θ with transverse co-moving radial distances of D_{M1} and D_{M2} . The co-moving separation of the second object as measured from the first object is

$$r = \sqrt{d^2 D_{M1}^2 + D_{M2}^2 - 2d D_{M1} D_{M2} \cos \theta}, \quad (7)$$

where

$$d = \sqrt{1 + \Omega_k \left(\frac{H_0 D_{M1}}{c} \right)^2} + \frac{D_{M1} \cos \theta}{D_{M2}} \left(1 - \sqrt{1 + \Omega_k \left(\frac{H_0 D_{M2}}{c} \right)^2} \right) \quad (8)$$

(e.g., Osmer 1981; Matarrese et al. 1997). In a flat universe $\Omega_k = 0$, $d = 1$ and Equation 7 reduces to the cosine rule for Euclidean space. Note that Equation 7 is not symmetric for the positions of the two objects. However, this is only important in the case in which d is not close to unity.

3.2. Construction of Random Samples

Generating random samples for the survey volume is critical for estimating the correlation function. The objective is to construct simulated datasets with constituents that are consistent with the physical distribution of the source population and are selected in the same manner as the real data. In the following Monte Carlo procedure we create an X-ray flux-limited sample of simulated AGN possessing the same flux and redshift distributions as the actual *ROSAT* NEP AGN. Of course the important difference between the simulated and real AGN is that the parent population of the former is assumed to be randomly distributed on the sky and in redshift space.

To properly model the non-uniform sensitivity pattern of the *ROSAT* NEP survey region (Figure 2), the simulated AGN must have the same flux distribution as the real AGN. We have demonstrated in §2.2 that the observed AGN flux distribution follows a power law of the form $N(> S) = KS^{-\alpha}$ where $\alpha \approx 1.3$ (Figure 4). Thus the differential probability distribution of fluxes scales like $S^{-(\alpha+1)}$. In practice the required set of random numbers with a power-law distribution is obtained from a set of random uniform numbers using a transformation method (e.g., Bevington & Robinson 1992). If p is a random number uniformly distributed between 0 and 1, then a random sampling in X-ray flux S above a limiting flux S_{lim} is distributed like

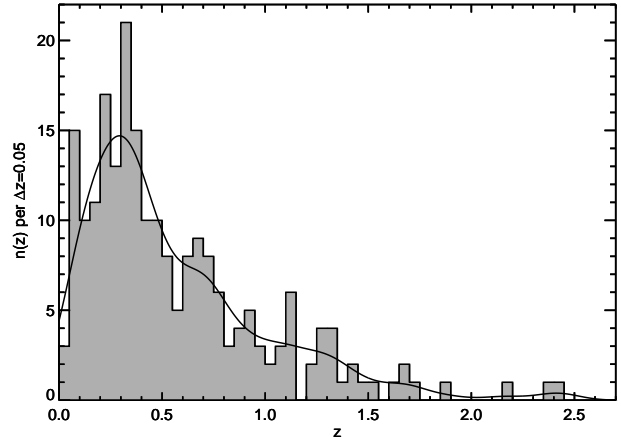


FIG. 5.— Redshift distribution of the *ROSAT* NEP AGN. The black line is the distribution smoothed with a Gaussian of width $\sigma_z = 0.1$. The median redshift of the sample is $z = 0.41$. To preserve the readability of this plot, the most distant AGN at $z = 3.889$ is not shown.

$$S = S_{\text{lim}} (1 - p)^{-1/\alpha}. \quad (9)$$

The limiting flux in the *ROSAT* NEP Survey for AGN is $S_{\text{lim}} = 2.0 \times 10^{-14} \text{ erg s}^{-1} \text{ cm}^{-2}$. Small variations to the value of α do not change the outcome of the clustering analysis.

Redshifts for the simulated AGN are drawn from a probability density function based on the observed distribution of the *ROSAT* NEP AGN (Figure 5). Here the redshift distribution has been smoothed with a Gaussian of width $\sigma_z = 0.1$. This smoothing scale is selected such that the resulting distribution has the overall shape of the data but is not strongly affected by discrete large-scale structure or Poisson fluctuations. Our results are insensitive to reasonable variations in this smoothing length.

We randomly place simulated AGN within the *ROSAT* NEP Survey boundaries ($17^h 15^m < \alpha_{2000} < 18^h 45^m$, $62^\circ < \delta_{2000} < 71^\circ$). For each object we assign an X-ray flux according to Equation 9 and a redshift drawn from the smoothed distribution. Then we test to see if its flux is above the local flux limit for its particular position in the survey region as shown in Figure 2. Objects above the threshold are retained, while those below are rejected. We proceed to randomly populate the survey volume in this manner until we have constructed a random catalog of 100,000 simulated AGN; i.e., ~ 450 times the size of the *ROSAT* NEP AGN sample.

4. RESULTS

We present the spatial correlation function of the *ROSAT* NEP AGN in Figure 6. Here the data and simulated objects have been binned up in terms of their pair separations (e.g., $DD(r)$, $RR(r)$, $DR(r)$) and evaluated using the adopted correlation estimator (Equation 5). The uncertainties associated with these data points are typically estimated using Poisson statistics of the form,

$$\delta \xi(r) = \frac{1 + \xi(r)}{\sqrt{DD(r)}} \quad (10)$$

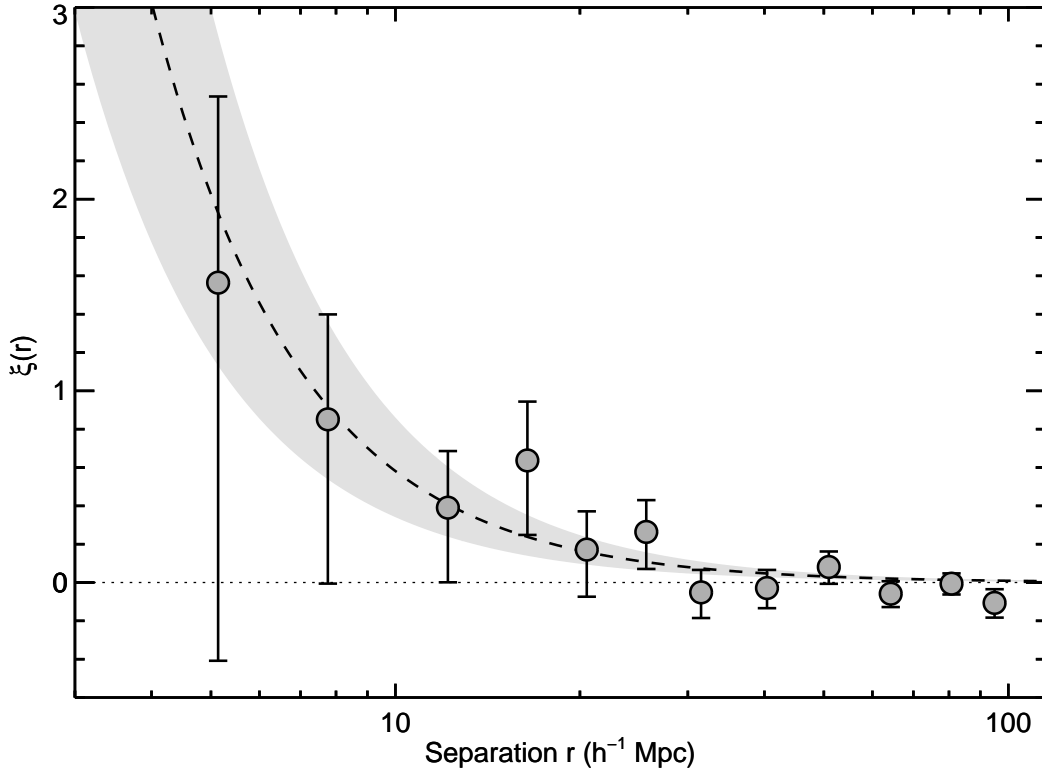


FIG. 6.— Spatial correlation function of the *ROSAT* NEP AGN. The error bars on the data points are 1σ Poisson errors. The dashed line is the maximum-likelihood fit ($r_0 = 7.4^{+1.8}_{-1.9} h^{-1}$ Mpc, $\gamma = 1.8$ fixed) to the range from 5 to $60 h^{-1}$ Mpc ($\Omega_M = 0.3$ and $\Omega_\Lambda = 0.7$). The shaded region demonstrates the $\pm 1\sigma$ errors on the correlation strength.

where $DD(r)$ is the number of data-data pairs in the interval. However, the Poisson distribution is not well approximated by a Gaussian in situations where the number of counts in each bin is small ($N \lesssim 20$) and thus the \sqrt{N} errors in the denominator of Equation 10 can underestimate the 68% confidence level. To avoid this we use the formulas of Gehrels (1986) to estimate the Poisson confidence intervals for one-sided 84% upper and lower bounds which correspond to $\pm 1\sigma$ in Gaussian statistics.

A positive clustering signal is readily apparent in the spatial correlation function of *ROSAT* NEP AGN and is significant at the 4σ level based on the excess AGN pairs relative to random at $r \lesssim 60 h^{-1}$ Mpc. Thus it is desirable to estimate the correlation strength and slope using the canonical power-law fit. This could be done using the coarsely binned data in Figure 6 and minimizing the χ^2 statistic. However, this approach is subject to uncertainties because the determination can be sensitive to the size and distribution of the selected bins. The maximum-likelihood method is an alternative means for determining a power-law fit to the correlation function which has the advantage of making maximal use of the data and is free from arbitrary binning (e.g., Croft et al. 1997; Popowski et al. 1998; Borgani, Plionis, & Kolokotronis 1999; Moscardini et al. 2000; Collins et al. 2000). The co-moving separation r is parsed into very small intervals such that there is either 0 or 1 object pair in any given interval. In this limit Poisson probabilities are appropriate. The probability P of observing ν_i object pairs

where μ_i pairs are expected is given by

$$P_{\mu_i}(\nu_i) = \frac{e^{-\mu_i} \mu_i^{\nu_i}}{\nu_i!}. \quad (11)$$

In the sparse sampling limit, the probabilities associated with the bins are independent of each other such that a likelihood function \mathcal{L} can be defined in terms of the joint probabilities,

$$\mathcal{L} = \prod_i \frac{e^{-\mu_i} \mu_i^{-\nu_i}}{\nu_i!}. \quad (12)$$

This leads to the useful expression

$$\ln \mathcal{L} = \sum_i (-\mu_i + \nu_i \ln \mu_i - \ln \nu_i!). \quad (13)$$

Here the summation is over all the intervals r_i within the range of co-moving separations for which the power-law fit is to be determined. The number of observed object pairs ν_i are the data-data pairs measured from the *ROSAT* NEP AGN, whereas the expected numbers of pairs μ_i are calculated using the Landy & Szalay estimator in Equation 5. Notice that μ_i , which is $DD(r_i)$ in Equation 5, is a function of the power-law parameters r_0 and γ and the pairwise data from the observed and random samples, specifically $DR(r_i)$ and $RR(r_i)$.

The best-fitting values of the power-law fit to the correlation function are determined by minimizing the expression

$$S = -2 \ln \mathcal{L} \quad (14)$$

with the confidence levels defined to be

$$\Delta S = S(r_0, \gamma) - S(r_{0,\text{best}}, \gamma_{\text{best}}). \quad (15)$$

Since S is distributed like χ^2 , the 1σ , 2σ , and 3σ (68.3%, 95.4%, and 99.7%) confidence intervals for a two parameter fit are $\Delta S = 2.30, 6.17$, and 11.8 , respectively (Avni 1976; Cash 1976, 1979). If we fix the slope, the confidence intervals for the one-parameter fit are $\Delta S = 1.0, 4.0$, and 9.0 .

We show the results of the maximum-likelihood analysis of the *ROSAT* NEP AGN clustering data in Figure 7. The power-law fit over the range from 5 to $60 h^{-1}$ Mpc indicates best-fit values of $r_0 = 7.5^{+2.7}_{-4.2} h^{-1}$ Mpc and $\gamma = 1.85^{+1.90}_{-0.80}$ where the errors are 1σ for two interesting parameters. If we set the slope at $\gamma = 1.8$ (the value typically found for normal galaxies and optically selected AGN), the correlation length is $r_0 = 7.4^{+1.8}_{-1.9} h^{-1}$ Mpc. We overplot this best-fit power-law on the pairwise data in Figure 6. The lower limit on the fitting range is set by the smallest AGN-AGN separation in the NEP data; the upper limit matches the general break in the power-law shape of the observed function. Our results do not change significantly for reasonable variations in the fitting range. For example, varying the upper limit between $40 h^{-1}$ Mpc and $80 h^{-1}$ Mpc results in the best-fit r_0 for $\gamma = 1.8$ ranging between $7.3 h^{-1}$ Mpc and $7.6 h^{-1}$ Mpc (i.e., $\Delta r_0 \lesssim 0.2\sigma$). Note that the effective redshift of the NEP clustering signal is $z_\xi = 0.22$ given by the median redshift of the AGN in pairs with separations in the range $5\text{--}60 h^{-1}$ Mpc. This characteristic redshift is smaller than the sample median ($z=0.41$) since the density of detected objects, and thus the number of close pairs, decreases with redshift in this flux-limited survey.

Repeating this analysis assuming an Einstein-de Sitter cosmology ($\Omega_M = 1, \Omega_\Lambda = 0$), we find best-fit values of $r_0 = 7.2^{+2.3}_{-4.0} h^{-1}$ Mpc and $\gamma = 1.83^{+1.66}_{-1.00}$, and $r_0 = 7.1 \pm 1.6 h^{-1}$ Mpc with $\gamma = 1.8$. This modest decrease in the correlation length is expected since the effect of a significant Ω_Λ is to increase object-object separations r and thus the resulting correlation length r_0 . These results are in excellent agreement with the preliminary analysis of the NEP data first reported in Mullis (2001).

There is a substantial supercluster of galaxies at $z = 0.087$ in the *ROSAT* NEP Survey region (Mullis et al. 2001). This is manifested as 5σ spikes in the redshift distributions of galaxy clusters and *IRAS* galaxies, but only a 2σ fluctuation in AGN density. There are 12 AGN from our sample in the redshift regime of the NEP supercluster ($0.07 < z < 0.1$). These objects comprise 5% of the total sample and 12% of the AGN at $z < 0.4$. We have examined the potential impact of the superstructure on the clustering signal by restricting the analysis to the 200 AGN at $z > 0.1$. This result is entirely consistent with the results from the analysis of the full sample ($\Delta r_0 \sim 0.6\sigma, \Delta\gamma \sim 0.2\sigma$). Thus the NEP supercluster has no significant effect on our results.

A final concern lies in the potential consequences of source confusion as a result of the angular resolution of the *ROSAT* PSPC detector. The FWHM of the

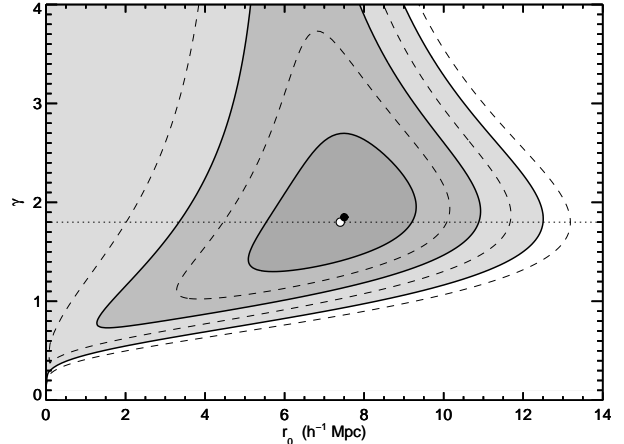


FIG. 7.— Probability contours for the power-law normalization (r_0) and slope (γ) from a maximum-likelihood analysis of the *ROSAT* NEP AGN ($\Omega_M = 0.3$ and $\Omega_\Lambda = 0.7$). The solid contours with shading are the 1σ , 2σ , and 3σ (68.3%, 95.4%, and 99.7%) confidence intervals for a two parameter fit. The dashed contours are the corresponding intervals for a one parameter fit. The filled circle marks the best-fit for two free parameters, $r_0 = 7.5^{+2.7}_{-4.2} h^{-1}$ Mpc and $\gamma = 1.85^{+1.90}_{-0.80}$; the open circle marks the best-fit for one free parameter with the slope fixed at $\gamma = 1.8$, $r_0 = 7.4^{+1.8}_{-1.9} h^{-1}$ Mpc. The dotted horizontal line indicates the canonical power-law slope for the correlation function ($\gamma \approx 1.8$).

RASS PSF is $\sim 35''$, and thus we expect sources separated by less than $\sim 30''$ to be unresolved. However, the confusion-limited regime is never approached due to the relative sparsity of AGN at the sensitivity limits of the *ROSAT* NEP Survey. For example, the smallest distance between two NEP AGN is $3.8'$. Furthermore, at the typical redshift of AGN contributing to the correlation detection ($z_\xi = 0.22$), $30''$ corresponds to a co-moving separation of $56 h^{-1}$ kpc which is much smaller than the best-fit correlation length. Thus confusion effects should not bias the correlation analysis.

5. DISCUSSION

In this section we discuss the significance of the *ROSAT* NEP results for the clustering of AGN, make comparisons to similar measures, and discuss the implications of our results for the evolution of AGN clustering.

5.1. First Direct Measure of the Spatial Correlation Function of X-ray Selected AGN

Our results from the analysis of *ROSAT* NEP data represent the first direct and significant measure of the spatial correlation function of X-ray selected AGN. This outcome is due to the advantageous combination of relatively deep sensitivity over a wide, contiguous survey region which results in sufficient numbers of AGN-AGN pairs at small scales to yield a significant signal. For example, the maximal signal-to-noise ratio in the pairwise data is observed at co-moving separations of less than $30 h^{-1}$ Mpc. Here we find 123 AGN-AGN pairs where only 78 pairs are expected if the data had a uniform spatial distribution. Thus AGN clustering is detected at greater than 4σ level.

The correlation length derived from the *ROSAT* NEP AGN sample is consistent with the value $r_0 \sim 6 h^{-1}$ Mpc

associated with normal galaxies (e.g., Hawkins et al. 2003) and optically selected AGN (e.g., Croom et al. 2001). This suggests that X-ray luminous AGN are spatially clustered in a manner similar to that of the aforementioned objects. In fact it lends additional evidence to the idea that X-ray selected and optically selected AGN are drawn from the same population. Our observations imply that AGN are not biased relative to galaxies based on the similarity of clustering strengths. Note that the factor of two density enhancement observed in *both* AGN and galaxies within the NEP supercluster provides further support to this view (see Figure 1 in Mullis et al. 2001). As observation and theory indicate the bias of local galaxies is close to unity (e.g., Verde et al. 2002; Weinberg et al. 2004, and references therein), the inferred bias parameter for X-ray selected AGN is also near unity, $b_X \sim 1$. Previous measurements of the X-ray bias, some of which included all extragalactic sources, have varied widely (see Barcons et al. 2001, and references therein); however our NEP measurement is in good agreement with recent results based on the hard X-ray background (Boughn & Crittenden 2004).

It is pertinent to review the two efforts to measure the spatial correlation of X-ray selected AGN prior to that of the NEP. The fact that there are such few studies reflects the difficulty of constructing sufficiently large and appropriately distributed samples to make this measure. The first clustering analysis of this type was performed by Boyle & Mo (1993) using 183 AGN ($z < 0.2$) taken from the *Einstein* Extended Medium Sensitivity Survey (EMSS; Stocke et al. 1991). Though this sample is similar in size to the NEP, it is spread over a nearly ten times larger solid angle (770 deg²). Moreover, their survey region is not contiguous, but rather the combination of hundreds of pointings distributed across the sky. Boyle & Mo (1993) found the significance of the clustering signal was only 0.8σ and concluded that AGN clustering at small scales is very weak, if present at all.

The second work to pursue the spatial correlation function is that of Carrera et al. (1998) who examined two separate samples of X-ray selected AGN. The first consisted of 107 objects ($0 < z < 3.5$, $\bar{z} = 1.43$) from the *ROSAT* Deep Survey (DRS; Shanks et al. 1991). The second was composed of 128 AGN ($0 < z < 3.5$, $\bar{z} = 0.84$) from the *ROSAT* International X-ray Optical Survey (RIXOS; Mason et al. 2000). Like the EMSS, the solid angles surveyed by the DRS and RIXOS (1.4 deg² and 20 deg², respectively) are the summation of many individual pointed observations. Carrera et al. (1998) found no indication of clustering in the DRS sample, but detected clustering at $r < 40\text{--}80 h^{-1}$ Mpc in the RIXOS sample at about 1.7σ significance. Given the limitations of the data, the authors did not present an explicit correlation function. However, by combining the DRS and RIXOS AGN, they derived a correlation length in the range of $1.5 < r_0 < 5.5 h^{-1}$ Mpc dependent upon the assumed model of clustering evolution. These results for an Einstein-de Sitter cosmological model would increase by approximately 30% in the concordance model.

Aside from our *ROSAT* NEP results, the only other significant measure of this kind to date is from the recent analysis of the *Chandra* deep fields. Gilli et al. (2004) have measured the projected correlation function ($w(r_p)$) where r_p is the co-moving separation perpendicular to

the line of sight) using the 2Msec *Chandra* Deep Field North (CDFN) and 1Msec *Chandra* Deep Field South (CDFS). This work is based on 160 AGN from the CDFN (mean redshift, $z \sim 0.96$) and 97 AGN from the CDFS ($z \sim 0.84$). Though these samples are smaller than that of the NEP, they are concentrated in much smaller solid angles, ~ 0.1 deg² each. Thus Gilli et al. are able to extract high signal-noise results by probing the correlation function at very small scales ($\sim 0.2\text{--}10 h^{-1}$ Mpc) where the signal is comparatively stronger. Converting the projected correlation to the three-dimension scale length assuming a power-law shape, they find for the CDFN $r_0 = 5.5 \pm 0.6 h^{-1}$ Mpc, $\gamma = 1.50 \pm 0.12$; for the CDFS $r_0 = 10.3 \pm 1.7 h^{-1}$ Mpc, $\gamma = 1.33 \pm 0.14$. If the slope is fixed at their preferred value of $\gamma = 1.4$, they find for the CDFN $r_0 = 5.1_{-0.5}^{+0.4} h^{-1}$ Mpc and for the CDFS $r_0 = 10.4 \pm 0.8 h^{-1}$ Mpc. There is a large variance between the two fields. However the strong enhancement in the correlation strength of the CDFS is attributed to two large redshift spikes at $z \sim 0.7$.

It is enlightening to compare the *ROSAT* NEP and CDFN/S spatial correlation functions. The clustering strength of the NEP, $r_0 \approx 7.4 h^{-1}$ Mpc, lies intermediate in the $r_0 = 5\text{--}10 h^{-1}$ Mpc range of the *Chandra* deep fields. The *ROSAT* AGN are a soft X-ray (0.1–2.4 keV) selected sample compared to the *Chandra* samples assembled from detections at both soft to hard energies (0.5–10 keV). Consequently the *ROSAT* NEP sample is dominated by type 1 AGN, whereas those of CDFN/S are composed of nearly equal mixes of type 1 and type 2 AGN. However, Gilli et al. (2004) have measured the correlation strength separately for hard versus soft detected AGN as well as type 1 versus type 2 AGN and find no significant differences. In relative terms, the NEP AGN are luminous and nearby while the CDFN/S AGN are faint and distant. The NEP characterizes the local ($z \sim 0.2$) clustering of AGN versus the distant ($z \sim 0.9$) measures of the CDFN/S, a point we will elaborate on in §5.3. The median luminosity of the *ROSAT* NEP AGN is $L_X = 9.2 \times 10^{43} h_{70}^{-2}$ ergs s⁻¹ whereas the mean of the CDFN/S is $L_X = 6.0 \times 10^{42} h_{70}^{-2}$ ergs s⁻¹ (both in the 0.5–2.0 keV energy band).

5.2. Comparison to the Angular Clustering of X-ray Sources

Thus far we have restricted our discussion to the direct measure of the spatial correlation of AGN using X-ray flux-limited samples. There are very few investigations of this kind due to the observational challenges of securing X-ray data of sufficient depth and/or breadth, and obtaining optical follow-up observations for object identifications and spectroscopic redshifts. If we allow for additional assumptions and uncertainties, the *angular* correlation function of X-ray sources can be incorporated.

The angular clustering of X-ray sources has been detected several times (e.g., Vikhlinin & Forman 1995; Akylas et al. 2000; Giacconi et al. 2001; Basilakos et al. 2004). The bulk of this signal is presumably generated by AGN since they are the dominant class of X-ray emitters at high Galactic latitudes. However, in the absence of optical follow-up, the exact AGN fraction is uncertain. The completely identified *ROSAT* NEP Survey provides a reference point at soft energies (0.5–2.0 keV) and at mod-

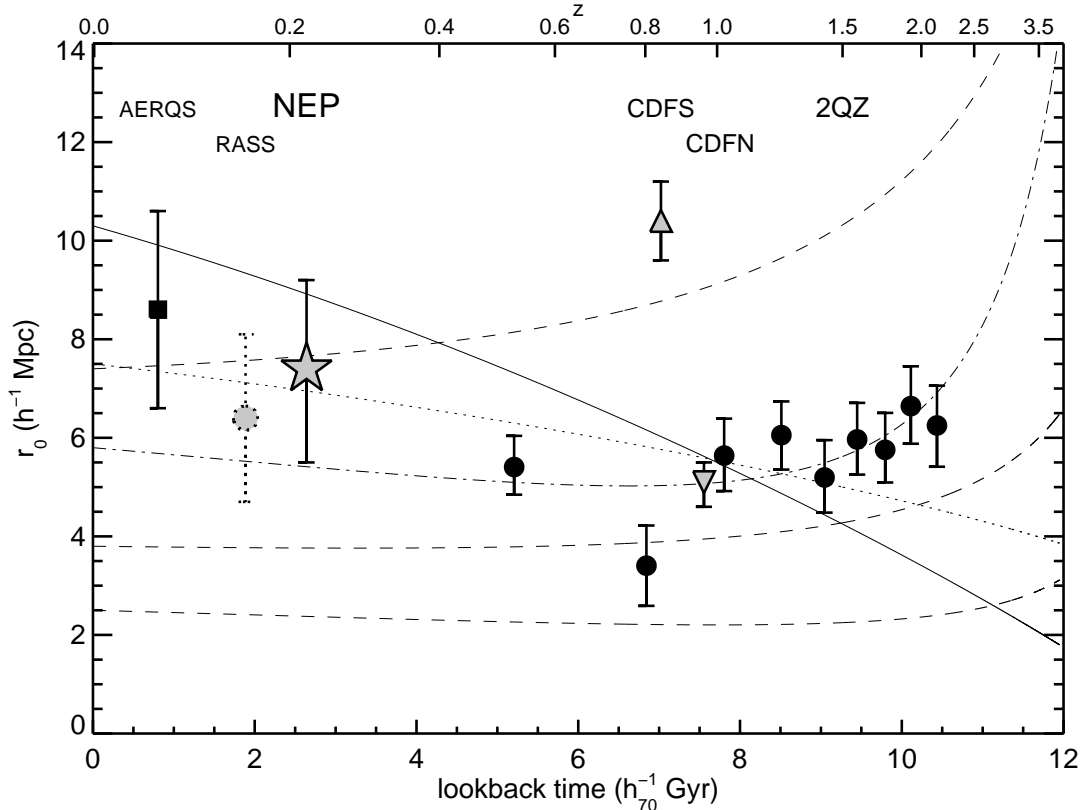


FIG. 8.— The scale length of AGN clustering as a function of lookback time (lower axis) and redshift (upper axis). X-ray results are shaded symbols; optical results are solid symbols. Symbol key and references for the data are: AERQS (filled square; Grazian et al. 2004), RASS (shaded circle; Akylas et al. 2000), NEP (shaded star; Mullis et al. 2001, and this paper), CDFN/S (shaded triangles; Gilli et al. 2004), and 2QZ (filled circles; Croom et al. 2003). All of these are from direct measures of the spatial correlation function except for the RASS. Over-plotted are theoretical predictions based on different biasing models described by Croom et al. (2001, and references therein): linear theory (solid line), long-lived AGN (dotted line), merger model for different values of the minimum halo mass (dashed line, $10^{12} M_{\odot}$, $10^{13} M_{\odot}$, $10^{14} M_{\odot}$ bottom to top). The dot-dashed line is the best-fitting empirical bias model for the 2QZ data. The uncertainty intervals of the measurements are based on one-parameter fits. The NEP and RASS use a fixed slope of $\gamma = 1.8$; AERQS and 2QZ assume $\gamma = 1.56$. CDFN/S use their preferred value of $\gamma = 1.4$. All of the measurements and models are for a Λ CDM cosmological model.

erately faint fluxes (a few times 10^{-14} ergs $\text{cm}^{-2} \text{s}^{-1}$) where $\sim 50\%$ of the X-ray sources are AGN. A second important caveat concerning these angular studies is that both the redshift distribution of the sources and the redshift dependence of the clustering evolution must be assumed to extract the three-dimensional correlation length r_0 .

Vikhlinin & Forman (1995) reported the first detection of the angular clustering of discrete X-ray sources using a set of deep *ROSAT* observations. They concluded that the correlation strength is consistent with that of optically selected AGN assuming such objects constitute a large fraction ($\gtrsim 50\%$) of their X-ray sources. Akylas et al. (2000) measured the angular clustering of X-ray sources from the RASS Bright Source Catalog, taking precautions to exclude stellar and extended sources as much as possible. Assuming a typical redshift of $z \sim 0.1-0.2$, comoving clustering evolution, and a power-law slope of $\gamma \approx 1.8$, they derived a correlation length of $r_0 \approx 6.4 \pm 1.7 h^{-1}$ Mpc; thus similar to the results at high redshift from optical surveys. We have converted their EdS result to Λ CDM assuming a median redshift of $z = 0.15$.

Recently Basilakos et al. (2004) analyzed the clustering of *XMM-Newton* hard X-ray sources (2–8 keV) in

a 2 deg^2 region. Exploring a variety of potential luminosity functions (and thus redshift distributions) and clustering characteristics, they found a rather high correlation length spanning the range $r_0 \sim 9 - 19 h^{-1}$ Mpc for $\gamma = 1.8$. Basilakos et al. argue that hard-band sources are more strongly correlated than soft-band sources. This claim is supported by the counts-in-cell analysis from deep *Chandra* data by Yang et al. (2003), but is at odds with the results of Gilli et al. (2004) for the CDFN/S.

5.3. Evolution of AGN Clustering

To round out this discussion, we incorporate the latest results on the clustering of *optically selected* AGN, and use the ensemble of X-ray and optical data to constrain the evolution of AGN clustering.

As outlined in § 1, there is a significant body of work in the literature characterizing the clustering of optically selected AGN. The current state of the art is encapsulated in the work of Croom et al. (2001, 2003) with the 2QZ survey. Analyzing a sample of over 20,000 AGN, they find the two-point spatial correlation has a power-law shape over the range $1 - 60 h^{-1}$ Mpc. Their best-fit parameters are $r_0 = 5.76_{-0.27}^{+0.17} h^{-1}$ Mpc and $\gamma = 1.64_{-0.03}^{+0.06}$ (Λ CDM) measured at a mean redshift of redshift $\bar{z} \approx 1.5$.

Moreover, the 2QZ sample is sufficiently large to map out the variation in clustering strength at high redshifts. Croom et al. (2003) find no evolution in the clustering amplitude from $z \sim 0.5$ to $z \sim 2.2$.

Ironic in the era of high-redshift studies, the clustering properties of *local* AGN has only recently been measured directly (Mullis 2001; Grazian et al. 2004). Our *ROSAT* NEP analysis has an effective redshift of $z_\xi \sim 0.2$. Grazian et al. (2004) have determined a similar measure for optically selected AGN using data from the Asiago-ESO/RASS QSO Survey (AERQS). They find an amplitude of $r_0 = 8.6 \pm 2.0 h^{-1}$ Mpc (Λ CDM) at an effective redshift of $z_\xi = 0.06$. The AERQS and NEP results are in excellent agreement.

A composite view of the clustering evolution of AGN is shown in Figure 8. Here we plot the scale length of the spatial correlation as a function of redshift and lookback time; X-ray results are shaded symbols, optical results are solid symbols. Note that all of these are direct measures of the spatial correlation function except for the RASS data point (Akylas et al. 2000) which is a transformation of the angular signal. Any conclusions to be drawn from these data must be taken with due regard for several caveats that will be discussed shortly. However, for now we take the data points at face value.

To the zeroth order no evolution is observed in the clustering strength of AGN out to redshift $z \sim 2.2$. A straight line at $r_0 = 6 h^{-1}$ Mpc is a good fit to the data with only two points deviating by greater than 3σ . The CDFS is an obvious outlier, but, as noted before this high value is likely due to cosmic variance. Looking with more detail, a weighted mean of the local measures (NEP, RASS, and AERQS) indicates $r_0 = 7.3 \pm 1.0 h^{-1}$ Mpc; whereas the high-redshift results (2QZ and CDFN/S) have a weighted mean of $r_0 = 5.80 \pm 0.21 h^{-1}$ Mpc. Thus there is an $\sim 25\%$ increase in clustering at low redshift ($z \sim 0.2$) relative to high redshift ($z \approx 1-2$). However, this very mild redshift evolution is significant at only the 1.4σ level.

The conclusion of zero to weak negative evolution is generally applicable to either the X-ray or optically selected AGN on their own, though with much less confidence for the former. Our *ROSAT* NEP results and the *Chandra* deep fields provide complementary redshift coverage. However, the trend based on strictly these X-ray AGN is still open ended due to the high variance of CDFN/S results. Forthcoming analysis at high redshift from *Chandra* and *XMM-Newton* will hopefully remove this uncertainty. We anticipate future findings will favor correlation lengths of $r_0 \approx 6 h^{-1}$ Mpc on average.

Our interpretation of the clustering behavior shown in Figure 8 must be tempered by several potentially important issues, including: 1) X-ray versus optical selection of the AGN, 2) comparison of different AGN types, 3) comparison of different AGN luminosities, and 4) comparison of amplitudes derived for different power-law slopes. The first two concerns are strongly coupled. Both *soft* X-ray selection and optical selection preferentially detect the unobscured, type 1 AGN. Conversely, *hard* X-ray selection also recovers the obscured, type 2 AGN. Assuming the unified paradigm for AGN is true (i.e., type 1 versus 2 properties are mainly due to viewing geometry), there is no obvious reason to expect the two classes to cluster differently. This anticipation is supported by the

tests of Gilli et al. (2004) in the CDFN/S, though the strong angular clustering of hard X-ray sources claimed by Yang et al. (2003) and Basilakos et al. (2004) could be weak counter examples. Note that the veracity of AGN unification is debated, and arguments can be made for the independent evolution of the two AGN populations (e.g., Franceschini et al. 2002, and references therein). Except for the deviant CDFS result, X-ray and optical AGN cluster similarly at similar redshifts based on the data in Figure 8.

The third issue of comparing dissimilar luminosities is relevant if this property is correlated with the mass of the dark matter halo in which AGN reside. Many popular clustering models make this assumption though its validity is not yet observationally confirmed (e.g., Croom et al. 2002). First consider the median luminosities of the X-ray selected samples. The *ROSAT* NEP AGN, with a median luminosity of $L_X = 9.2 \times 10^{43} h_{70}^{-2}$ ergs s^{-1} , are on average about fifteen times more luminous than those from the CDFN/S ($L_X = 6.0 \times 10^{42} h_{70}^{-2}$ ergs s^{-1}). We estimate the median luminosity of the RASS AGN of Akylas et al. (2000) to be a few times 10^{43} , thus intermediate to the NEP and CDFN/S. It is interesting to note that the median X-ray luminosity of the *ROSAT* NEP AGN is rather similar to those that we estimate for the 2QZ and AERQS. Taking the mean absolute magnitudes of these two samples (2QZ: $M_B = -25.11$, Croom et al. 2002, AERQS: $M_B = -22.99$, Grazian et al. 2004, both $H_0 = 70$ km s^{-1} Mpc $^{-1}$, Λ CDM) and using an average spectral energy distribution (e.g., Elvis et al. 1994) or the observed X-ray/optical relation (e.g., Vignali et al. 2003), we find mean luminosities of $L_X \approx 4 \times 10^{44} h_{70}^{-2}$ ergs s^{-1} for the 2QZ and $L_X \approx 1 \times 10^{44} h_{70}^{-2}$ ergs s^{-1} for the AERQS.

The last complication to consider in regards to the data in Figure 8 lies in the fact that different authors use different values for the power-law slope of the correlation function in deriving the clustering amplitude. The NEP and RASS analyses, for example, are based on a fixed slope of $\gamma = 1.8$. The 2QZ and AERQS adopt a slope of $\gamma = 1.56$. The CDFN/S report single-parameter fits for their preferred value of $\gamma = 1.4$. Thus problems may arise in comparing the clustering strengths since the scale length and the slope are correlated to some degree. However, the magnitude of the effect appears to be manageable. For instance, in the case of the NEP these parameters are not strongly linked (see Figure 7). The NEP correlation length decreases by $\sim 14\%$ to $r_0 \approx 6.5 h^{-1}$ Mpc if we lower the slope to $\gamma = 1.56$. Similarly, Gilli et al. (2004) report their best-fit correlation lengths for the CDFN/S each increase by 15% if they assume a slope of $\gamma = 1.8$. Notice such adjustments to homogenize the surveys tend to erase the marginal evolution trend discussed above, and further strengthen the case for no redshift evolution.

The above caveats notwithstanding, we briefly outline possible theoretical interpretations of the clustering strength behavior as a function of redshift. The manner in which *mass* clusters via gravitational instability is generally well understood. Thus the spatial correlation function of matter fluctuations, ξ_{mass} , can be computed with little ambiguity (e.g., Smith et al. 2003). However, connecting this mass clustering to AGN clustering is non-

trivial since we do not know the distribution of AGN relative to the distribution of mass. This bias between the luminous and dark matter densities is parameterized by $b(z)$ and reflects the unknown physical mechanisms of AGN formation.

The evolution of the AGN correlation function is often formulated in the following terms,

$$\xi(r, z) = b^2(z) D^2(z) \xi_{\text{mass}}(r, z = 0). \quad (16)$$

Here $D(z)$ is the linear growth of density perturbations which is $(1+z)^{-1}$ for an EdS cosmology. The present-day spatial correlation function of mass is $\xi_{\text{mass}}(r, z = 0)$.

We introduce three models for consideration. The simplest scenario of clustering evolution assumes the bias does not change with redshift. The linear theory model scales like $D^2(z)$ and is represented by the solid line in Figure 8. The second model, the long-lived scenario, proposes that AGN are formed at an arbitrarily high redshift and then move thereafter according to the gravitational potential of the density fluctuations (Fry 1996). Here the bias parameter increases with redshift which counteracts the linear growth factor and produces negative evolution which is less steep than linear theory (dotted line in Figure 8). The third biasing scenario, known as the merger model, uses the Press-Schechter (1974) formalism to track the evolution of the dark matter halo mass function (Matarrese et al. 1997; Moscardini et al. 1998). The resulting bias parameter evolves more steeply than the growth of perturbations enabling a model clustering strength that increases with redshift. The overall strength of clustering reflects the mass of the dark matter halos hosting the AGN. The merger model predictions for several minimum halo masses are plotted in Figure 8 (dashed lines). More extensive discussions of these biasing models are laid out in Croom et al. (2001) and Grazian et al. (2004).

The linear model is clearly too steep and inconsistent with the flat to mildly negative evolution delineated by the clustering observations. The less steep long-lived model agrees with the local measures but can not replicate the flat behavior of the 2QZ data at high redshift. In terms of overall shape, the closest agreement is given by the merger model. The empirical biasing description of Croom et al. (2001) is based on the merger model. Their best fit with a minimum halo mass of $\sim 10^{13} h^{-1} M_{\odot}$ is shown as the dot-dashed line in Figure 8. The *ROSAT* NEP clustering strength is consistent with this model as are most of the other data, except for the CDFS.

6. CONCLUSIONS

We have made the first direct measurement of the spatial correlation of X-ray selected AGN. These results are based on the analysis of 219 AGN detected at soft energies (0.1–2.4 keV) in the *ROSAT* NEP Survey. The AGN catalog, presented here, includes updated X-ray and optical properties and features complete optical identifications and spectroscopic redshifts. The clustering signal is significant at the 4σ level corresponding to a cluster-

ing length of $r_0 = 7.4_{-1.9}^{+1.8} h^{-1}$ Mpc assuming a power-law shape with a slope $\gamma = 1.8$. The median redshift of the AGN contributing to this signal is $z_{\xi} = 0.22$.

Our results indicate that X-ray and optically selected AGN share similar clustering properties as both display clustering scale lengths of $r_0 \sim 6 h^{-1}$ Mpc. This is not too surprising given that soft X-ray and optical selection are preferentially sensitive to unobscured type 1 AGN. Assuming that we are probing the same population, the *ROSAT* NEP measure provides an effective zero-point in the study of clustering evolution. This low redshift determination is quite valuable since optical surveys are largely ineffective in this regime. The no-evolution trend delineated by the 2QZ at high redshifts appears to extend to low redshifts based on the NEP analysis. We find a modest increase in clustering strength ($\sim 25\%$) at $z \lesssim 0.2$ relative to the high redshift results at $z \sim 1.5$; however, this is only 1.4σ significant.

Since the amplitudes of galaxy and AGN clustering are similar, we argue that AGN are not biased relative to galaxies. It likely that AGN randomly sample the galaxy distribution and do not preferentially probe the high peaks of the matter density field. Given that the bias of local galaxies is near unity, the inferred X-ray bias is near unity. Hence it seems that X-ray selected AGN closely trace the underlying mass distribution.

The study of X-ray AGN clustering is still in the early stages and much work lies ahead. The NEP has provided the first firm data point, and the recent results from the CDFN/S provide small uncertainty but large variance measures at high redshift. Forthcoming results from on-going and planned deep surveys with *Chandra* and *XMM-Newton* will play a vital role by hopefully averaging out cosmic variance and securing the clustering amplitude at high redshift. Future X-ray survey missions like the Dark Universe Observatory will provide precision measures of X-ray AGN clustering as a function of high redshift with the *ROSAT* NEP results serving as an important anchor point at low redshift.

It is a pleasure to acknowledge Roberto Gilli, Emanuele Daddi, and Anna Wolter for stimulating discussions. We thank the first two for allowing us to quote their results for the CDFN/S prior to publication. We appreciate Giusi Micela and Jorge Sanz for providing additional observations to clarify the identification of RX J1824.7+6509. We thank the anonymous referee for the careful review of this work and for comments that improved the presentation. We are grateful to our sponsoring agencies. We are grateful to our sponsoring agencies. Support has come from the ESO Office for Science, NSF (AST 91-19216 and AST 95-00515), NASA (NGT5-50175, GO-5402.01-93A, and GO-05987.02-94A), the ARCS foundation, the Smithsonian Institution, NATO (CRG91-0415), the Italian Space Agency ASI-CNR, the Bundesministerium für Forschung (BMBF/DLR), and the Max-Planck-Gesellschaft (MPG).

REFERENCES

- Akylas, A., Georgantopoulos, I., & Plionis, M. 2000, MNRAS, 318, 1036
 Andreani, P. & Cristiani, S. 1992, ApJ, 398, L13
 Avni, Y. 1976, ApJ, 210, 642
 Avni, Y. & Tananbaum, H. 1986, ApJ, 305, 83

- Barcons, X., Carrera, F. J., Ceballos, M. T., & Mateos, S. 2001, in AIP Conf. Proc. 599: X-ray Astronomy: Stellar Endpoints, AGN, and the Diffuse X-ray Background, 3–12
- Basilakos, S., Georgakakis, A., Plionis, M., & Georgantopoulos, I. 2004, *ApJ*, 607, L79
- Bevington, P. R. & Robinson, D. K. 1992, *Data reduction and error analysis for the physical sciences* (New York: McGraw-Hill, —c1992, 2nd ed.)
- Borgani, S., Plionis, M., & Kolokotronis, V. 1999, *MNRAS*, 305, 866
- Boughn, S. & Crittenden, R. 2004, *ArXiv Astrophysics e-prints*
- Boyle, B. J. & Mo, H. J. 1993, *MNRAS*, 260, 925
- Carrera, F. J., Barcons, X., Fabian, A. C., Hasinger, G., Mason, K. O., McMahon, R. G., Mittaz, J. P. D., & Page, M. J. 1998, *MNRAS*, 299, 229
- Cash, W. 1976, *A&A*, 52, 307
- . 1979, *ApJ*, 228, 939
- Collins, C. A., Guzzo, L., Böhringer, H., Schuecker, P., Chincarini, G., Cruddace, R., De Grandi, S., MacGillivray, H. T., Neumann, D. M., Schindler, S., Shaver, P., & Voges, W. 2000, *MNRAS*, 319, 939
- Croft, R. A. C., Dalton, G. B., Efstathiou, G., Sutherland, W. J., & Maddox, S. J. 1997, *MNRAS*, 291, 305
- Croom, S., Boyle, B., Shanks, T., Outram, P., Smith, R., Miller, L., Loaring, N., Kenyon, S., & Couch, W. 2003, *ArXiv Astrophysics e-prints*
- Croom, S. M., Boyle, B. J., Loaring, N. S., Miller, L., Outram, P. J., Shanks, T., & Smith, R. J. 2002, *MNRAS*, 335, 459
- Croom, S. M. & Shanks, T. 1996, *MNRAS*, 281, 893
- Croom, S. M., Shanks, T., Boyle, B. J., Smith, R. J., Miller, L., Loaring, N. S., & Hoyle, F. 2001, *MNRAS*, 325, 483
- Davis, M. & Peebles, P. J. E. 1983, *ApJ*, 267, 465
- Elvis, M., Lockman, F. J., & Fassnacht, C. 1994, *ApJS*, 95, 413
- Elvis, M., Maccacaro, T., Wilson, A. S., Ward, M. J., Penston, M. V., Fosbury, R. A. E., & Perola, G. C. 1978, *MNRAS*, 183, 129
- Engels, D., Hagen, H.-J., Cordis, L., Koehler, S., Wisotzki, L., & Reimers, D. 1998, *A&AS*, 128, 507
- Franceschini, A., Braitto, V., & Fadda, D. 2002, *MNRAS*, 335, L51
- Fry, J. N. 1996, *ApJ*, 461, L65
- Gehrels, N. 1986, *ApJ*, 303, 336
- Giacconi, R., Rosati, P., Tozzi, P., Nonino, M., Hasinger, G., Norman, C., Bergeron, J., Borgani, S., Gilli, R., Gilmozzi, R., & Zheng, W. 2001, *ApJ*, 551, 624
- Gilli, R., Daddi, E., Zamorani, G., Tozzi, P., Borgani, S., Bergeron, J., Giacconi, R., Hasinger, G., Mainieri, V., Norman, C., Rosati, P., Szokoly, G., & Zheng, W. 2004, *A&A*, submitted
- Gioia, I. M., Henry, J. P., Mullis, C. R., Böhringer, H., Briel, U. G., Voges, W., & Huchra, J. P. 2003, *ApJS*, 149, 29
- Grazian, A., Negrello, M., Moscardini, L., Cristiani, S., Haehnelt, M. G., Matarrese, S., Omizzolo, A., & Vanzella, E. 2004, *AJ*, 127, 592
- Hamilton, A. J. S. 1993, *ApJ*, 417, 19
- Hartwick, F. D. A. & Schade, D. 1990, *ARA&A*, 28, 437
- Hasinger, G., Burg, R., Giacconi, R., Hartner, G., Schmidt, M., Trumper, J., & Zamorani, G. 1993, *A&A*, 275, 1
- Hawkins, E., Maddox, S., Cole, S., Lahav, O., Madgwick, D. S., Norberg, P., Peacock, J. A., Baldry, I. K., Baugh, C. M., Bland-Hawthorn, J., Bridges, T., Cannon, R., Colless, M., Collins, C., Couch, W., Dalton, G., De Propriis, R., Driver, S. P., Efstathiou, G., Ellis, R. S., Frenk, C. S., Glazebrook, K., Jackson, C., Jones, B., Lewis, I., Lumsden, S., Percival, W., Peterson, B. A., Sutherland, W., & Taylor, K. 2003, *MNRAS*, 346, 78
- Henry, J. P., Gioia, I. M., Mullis, C. R., Voges, W., Briel, U. G., Böhringer, H., & Huchra, J. P. 2001, *ApJ*, 553, L109
- Hewett, P. C. 1982, *MNRAS*, 201, 867
- Hogg, D. W. 1999, *ArXiv Astrophysics e-prints*
- Iovino, A. & Shaver, P. A. 1988, *ApJ*, 330, L13
- Kerscher, M., Szapudi, I., & Szalay, A. S. 2000, *ApJ*, 535, L13
- La Franca, F., Andreani, P., & Cristiani, S. 1998, *ApJ*, 497, 529
- Landy, S. D. & Szalay, A. S. 1993, *ApJ*, 412, 64
- Mason, K. O., Carrera, F. J., Hasinger, G., Andernach, H., Aragon-Salamanca, A., Barcons, X., Bower, R., Brandt, W. N., Branduardi-Raymont, G., Burgos-Martín, J., Cabrera-Guerra, F., Carballo, R., Castander, F., Ellis, R. S., González-Serrano, J. I., Martínez-González, E., Martín-Mirones, J. M., McMahon, R. G., Mittaz, J. P. D., Nicholson, K. L., Page, M. J., Pérez-Fournon, I., Puchnarewicz, E. M., Romero-Colmenero, E., Schwöpe, A. D., Vila, B., Watson, M. G., & Wonnacott, D. 2000, *MNRAS*, 311, 456
- Matarrese, S., Coles, P., Lucchin, F., & Moscardini, L. 1997, *MNRAS*, 286, 115
- Mo, H. J. & Fang, L. Z. 1993, *ApJ*, 410, 493
- Moscardini, L., Coles, P., Lucchin, F., & Matarrese, S. 1998, *MNRAS*, 299, 95
- Moscardini, L., Matarrese, S., De Grandi, S., & Lucchin, F. 2000, *MNRAS*, 314, 647
- Mullis, C. R. 2001, Ph.D. Thesis, Univ. of Hawaii
- Mullis, C. R., Henry, J. P., Gioia, I. M., Böhringer, H., Briel, U. G., Voges, W., & Huchra, J. P. 2001, *ApJ*, 553, L115
- Murdoch, H. S., Crawford, D. F., & Jauncey, D. L. 1973, *ApJ*, 183, 1
- Mushotzky, R. 2004, *ArXiv Astrophysics e-prints*
- Osmer, P. S. 1981, *ApJ*, 247, 762
- Peebles, P. J. E. 1980, *The large-scale structure of the universe* (Princeton, N.J., Princeton University Press)
- . 1993, *Principles of Physical Cosmology* (Princeton, NJ: Princeton University Press)
- Popowski, P. A., Weinberg, D. H., Ryden, B. S., & Osmer, P. S. 1998, *ApJ*, 498, 11
- Press, W. H. & Schechter, P. 1974, *ApJ*, 187, 425
- Shanks, T. & Boyle, B. J. 1994, *MNRAS*, 271, 753
- Shanks, T., Fong, R., Boyle, B. J., & Peterson, B. A. 1987, *MNRAS*, 227, 739
- Shanks, T., Georgantopoulos, I., Stewart, G. C., Pounds, K. A., Boyle, B. J., & Griffiths, R. 1991, *Nature*, 353, 315
- Shaver, P. A. 1984, *A&A*, 136, L9
- Smith, R. E., Peacock, J. A., Jenkins, A., White, S. D. M., Frenk, C. S., Pearce, F. R., Thomas, P. A., Efstathiou, G., & Couchman, H. M. P. 2003, *MNRAS*, 341, 1311
- Stark, A. A., Gammie, C. F., Wilson, R. W., Bally, J., Linke, R. A., Heiles, C., & Hurwitz, M. 1992, *ApJS*, 79, 77
- Stoeck, J. T., Morris, S. L., Gioia, I. M., Maccacaro, T., Schild, R., Wolter, A., Fleming, T. A., & Henry, J. P. 1991, *ApJS*, 76, 813
- Verde, L., Heavens, A. F., Percival, W. J., Matarrese, S., Baugh, C. M., Bland-Hawthorn, J., Bridges, T., Cannon, R., Cole, S., Colless, M., Collins, C., Couch, W., Dalton, G., De Propriis, R., Driver, S. P., Efstathiou, G., Ellis, R. S., Frenk, C. S., Glazebrook, K., Jackson, C., Lahav, O., Lewis, I., Lumsden, S., Maddox, S., Madgwick, D., Norberg, P., Peacock, J. A., Peterson, B. A., Sutherland, W., & Taylor, K. 2002, *MNRAS*, 335, 432
- Vignali, C., Brandt, W. N., & Schneider, D. P. 2003, *AJ*, 125, 433
- Vikhlinin, A. & Forman, W. 1995, *ApJ*, 455, L109
- Voges, W., Henry, J. P., Briel, U. G., Böhringer, H., Mullis, C. R., Gioia, I. M., & Huchra, J. P. 2001, *ApJ*, 553, L119
- Weinberg, D. H., Davé, R., Katz, N., & Hernquist, L. 2004, *ApJ*, 601, 1
- Weinberg, S. 1972, *Gravitation and Cosmology: Principles and Applications of the General Theory of Relativity* (New York: John Wiley & Sons)
- Yang, Y., Mushotzky, R. F., Barger, A. J., Cowie, L. L., Sanders, D. B., & Steffen, A. T. 2003, *ApJ*, 585, L85
- Zehavi, I., Blanton, M. R., Frieman, J. A., Weinberg, D. H., Mo, H. J., Strauss, M. A., Anderson, S. F., Annis, J., Bahcall, N. A., Bernardi, M., Briggs, J. W., Brinkmann, J., Burles, S., Carey, L., Castander, F. J., Connolly, A. J., Csabai, I., Dalcanton, J. J., Dodelson, S., Doi, M., Eisenstein, D., Evans, M. L., Finkbeiner, D. P., Friedman, S., Fukugita, M., Gunn, J. E., Hennessy, G. S., Hindsley, R. B., Ivezić, Ž., Kent, S., Knapp, G. R., Kron, R., Kunszt, P., Lamb, D. Q., Leger, R. F., Long, D. C., Loveday, J., Lupton, R. H., McKay, T., Meiksin, A., Merrelli, A., Munn, J. A., Narayanan, V., Newcomb, M., Nichol, R. C., Owen, R., Peoples, J., Pope, A., Rockosi, C. M., Schlegel, D., Schneider, D. P., Scoccimarro, R., Sheth, R. K., Siegmund, W., Smee, S., Snir, Y., Stebbins, A., Stoughton, C., SubbaRao, M., Szalay, A. S., Szapudi, I., Tegmark, M., Tucker, D. L., Uomoto, A., Vanden Berk, D., Vogeley, M. S., Waddell, P., Yanny, B., & York, D. G. 2002, *ApJ*, 571, 172

TABLE 1
ROSAT NEP AGN CATALOG

Object	NEP ID	α_X (J2000)	δ_X (J2000)	α_{opt} (J2000)	δ_{opt} (J2000)	n_H [10^{20} cm^{-2}]	Count Rate [s^{-1}]	Count Rate Error [s^{-1}]	f_X [10^{-14} cgs]	L_X [10^{44} cgs]	z	AGN Type
(1)	(2)	(3)	(4)	(5)	(6)	(7)	(8)	(9)	(10)	(11)	(12)	(13)
RX J1715.4+6239	1239	17 15 25.3	+62 39 34	17 15 25.7	+62 39 27	2.62	0.0173	0.0038	13.94	4.88	0.8500	2
RX J1716.2+6836	1270	17 16 14.4	+68 36 36	17 16 13.8	+68 36 38	3.57	0.1192	0.0059	112.56	31.57	0.7770	1
RX J1717.1+6401	1272	17 17 08.1	+64 01 46	17 17 07.1	+64 01 45	2.97	0.0400	0.0043	34.41	0.16	0.1334	1
RX J1717.5+6559	1300	17 17 35.6	+65 59 35	17 17 37.9	+65 59 39	3.31	0.0467	0.0052	42.45	1.17	0.2936	1
RX J1717.7+6431	1320	17 17 44.4	+64 31 45	17 17 47.4	+64 31 41	3.61	0.0164	0.0029	15.59	0.004	0.0337	2
RX J1717.9+7038	1330	17 17 57.0	+70 38 15	17 17 56.6	+70 38 16	3.96	0.0492	0.0048	48.91	0.41	0.1738	2
RX J1718.0+6727	1340	17 18 05.5	+67 27 11	17 18 05.9	+67 27 00	3.77	0.0207	0.0028	20.09	2.43	0.5506	1
RX J1719.0+6929	1410	17 19 03.6	+69 29 33	17 19 03.5	+69 29 39	4.02	0.0129	0.0027	12.93	0.32	0.2816	1
RX J1720.1+6833	1450	17 20 07.8	+68 33 37	17 20 06.6	+68 33 50	3.64	0.0175	0.0027	16.71	1.92	0.5392	1
RX J1720.8+6210	1471	17 20 48.8	+62 10 13	17 20 42.3	+62 10 10	2.80	0.0251	0.0051	20.92	5.06	0.7313	1
RX J1721.0+6711	1490	17 21 03.1	+67 11 54	17 21 02.3	+67 11 57	3.77	0.0099	0.0021	9.61	2.50	0.7538	1
RX J1723.1+6826	1540	17 23 10.4	+68 26 54	17 23 09.9	+68 26 56	4.18	0.0082	0.0019	8.37	4.14	0.9782	1
RX J1724.9+6636	1640	17 24 55.5	+66 36 59	17 24 56.1	+66 36 50	3.84	0.0105	0.0026	10.29	2.08	0.6792	2
RX J1726.5+6714	1670	17 26 30.7	+67 14 12	17 26 28.6	+67 14 15	3.91	0.0108	0.0020	10.67	0.49	0.3659	1
RX J1726.7+6643	1680	17 26 43.9	+66 43 30	17 26 45.0	+66 43 19	3.73	0.0399	0.0044	38.55	1.82	0.3705	1
RX J1727.2+6322	1710	17 27 12.0	+63 22 44	17 27 11.7	+63 22 41	2.88	0.0818	0.0070	69.20	0.95	0.2169	1
RX J1727.8+6748	1740	17 27 49.5	+67 48 43	17 27 45.5	+67 48 43	4.16	0.0142	0.0021	14.47	1.36	0.4950	1
RX J1728.5+6732	1770	17 28 35.4	+67 32 33	17 28 34.6	+67 32 24	4.56	0.0071	0.0016	7.55	1.36	0.6493	1
RX J1729.2+7032	1782	17 29 12.0	+70 32 57	17 29 11.8	+70 32 55	3.88	0.0140	0.0032	13.78	1.58	0.5378	1
RX J1732.0+6926	1910	17 32 05.5	+69 26 22	17 32 04.5	+69 26 39	4.02	0.0148	0.0026	14.83	1.45	0.5043	1
RX J1732.5+7031	1920	17 32 31.3	+70 31 37	17 32 31.0	+70 31 31	3.88	0.0363	0.0045	35.73	0.47	0.2114	1
RX J1732.9+6533	1930	17 32 54.5	+65 33 24	17 32 53.9	+65 33 25	4.01	0.0344	0.0034	34.42	12.25	0.8560	1
RX J1734.5+6755	1980	17 34 30.3	+67 55 05	17 34 27.8	+67 55 04	4.83	0.0080	0.0017	8.73	0.14	0.2341	1
RX J1736.0+6559	2040	17 36 00.0	+65 59 00	17 36 01.9	+65 58 54	3.74	0.0094	0.0021	9.09	0.62	0.4341	1
RX J1737.0+6601	2131	17 37 05.5	+66 01 05	17 37 07.8	+66 01 02	3.76	0.0141	0.0021	13.68	0.60	0.3580	2
RX J1738.0+6210	2160	17 38 02.6	+62 10 42	17 38 03.8	+62 10 54	3.34	0.0115	0.0024	10.51	13.54	1.4402	1
RX J1738.4+6417	2180	17 38 24.0	+64 17 59	17 38 24.5	+64 17 56	2.77	0.0131	0.0024	10.87	3.23	0.7955	1
RX J1738.7+7037	2200	17 38 42.0	+70 37 05	17 38 42.0	+70 37 16	3.93	0.0289	0.0037	28.64	0.15	0.1399	1
RX J1739.3+6614	2211	17 39 21.5	+66 14 41	17 39 25.8	+66 14 31	3.66	0.0078	0.0019	7.46	8.13	1.3460	1
RX J1739.7+6710	2230	17 39 44.6	+67 10 52	17 39 44.7	+67 10 43	4.49	0.0339	0.0027	35.79	0.13	0.1180	1
RX J1739.9+7005	2240	17 39 56.0	+70 05 52	17 39 54.2	+70 05 57	3.93	0.0169	0.0028	16.75	1.78	0.5209	1
RX J1741.2+6507	2300	17 41 14.4	+65 07 43	17 41 15.7	+65 07 42	4.26	0.0133	0.0021	13.71	3.49	0.7466	1
RX J1741.7+6335	2320	17 41 46.0	+63 35 13	17 41 45.6	+63 35 22	2.75	0.0169	0.0026	13.95	65.61	2.4420	1
RX J1742.2+6639	2340	17 42 12.5	+66 39 49	17 42 13.8	+66 39 34	3.69	0.0132	0.0020	12.69	12.02	1.2720	1
RX J1742.2+6936	2341	17 42 15.1	+69 36 29	17 42 16.6	+69 36 21	3.71	0.0100	0.0023	9.63	5.64	1.0470	1
RX J1742.2+6351	2350	17 42 17.9	+63 51 09	17 42 18.4	+63 51 15	2.91	0.0389	0.0038	33.13	1.89	0.4019	1
RX J1742.7+6800	2371	17 42 42.0	+68 00 11	17 42 43.5	+68 00 16	3.99	0.0084	0.0016	8.38	0.02	0.0858	1
RX J1743.7+6829	2450	17 43 43.5	+68 29 26	17 43 42.9	+68 29 25	4.26	0.0066	0.0015	6.80	0.28	0.3504	1
RX J1743.8+6657	2460	17 43 49.2	+66 57 23	17 43 49.3	+66 57 08	4.13	0.0055	0.0013	5.58	0.51	0.4900	1
RX J1744.2+6534	2490	17 44 14.2	+65 34 54	17 44 14.5	+65 34 53	3.58	0.0544	0.0030	51.50	1.02	0.2550	1
RX J1744.9+6536	2550	17 44 55.0	+65 36 00	17 44 54.5	+65 36 02	3.59	0.0061	0.0012	5.78	0.24	0.3533	1
RX J1745.7+6748	2610	17 45 42.6	+67 48 15	17 45 42.4	+67 48 14	4.28	0.0058	0.0013	5.99	0.37	0.4143	2
RX J1745.9+6451	2650	17 45 55.2	+64 51 18	17 45 55.5	+64 51 25	3.49	0.0211	0.0024	19.70	0.18	0.1790	1
RX J1746.0+6727	2670	17 46 03.0	+67 27 09	17 46 01.8	+67 27 09	4.70	0.0120	0.0015	12.94	0.17	0.2146	1
RX J1746.1+6737	2700	17 46 09.6	+67 37 21	17 46 08.8	+67 37 15	4.21	0.1464	0.0044	149.98	0.06	0.0410	1
RX J1746.2+6227	2710	17 46 14.6	+62 27 01	17 46 13.9	+62 26 54	3.25	0.0319	0.0034	28.73	413.35	3.8890	1
RX J1746.3+6320	2750	17 46 21.6	+63 20 06	17 46 21.8	+63 20 10	3.02	0.0165	0.0026	14.31	0.67	0.3697	1
RX J1747.0+6836	2800	17 47 00.3	+68 36 26	17 46 59.9	+68 36 34	4.42	0.2131	0.0060	223.35	0.21	0.0630	1
RX J1747.1+6813	2810	17 47 10.6	+68 13 19	17 47 12.7	+68 13 26	4.54	0.0057	0.0013	6.05	27.06	2.3920	1
RX J1747.2+6532	2820	17 47 14.4	+65 32 30	17 47 13.9	+65 32 35	3.66	0.0108	0.0016	10.33	15.11	1.5166	1
RX J1747.3+6702	2840	17 47 22.2	+67 02 06	17 47 21.5	+67 02 01	4.51	0.0066	0.0011	6.99	1.75	0.7421	1
RX J1747.4+6626	2850	17 47 26.8	+66 26 27	17 47 27.0	+66 26 24	3.78	0.0138	0.0014	13.42	0.07	0.1391	1
RX J1747.4+6924	2860	17 47 27.0	+69 24 55	17 47 27.9	+69 25 09	3.49	0.0099	0.0020	9.25	1.02	0.5292	2

TABLE 1 — *Continued*

Object	NEP ID	α_X (J2000)	δ_X (J2000)	α_{opt} (J2000)	δ_{opt} (J2000)	n_H [10^{20} cm^{-2}]	Count Rate [s^{-1}]	Count Rate Error [s^{-1}]	f_X [10^{-14} cgs]	L_X [10^{44} cgs]	z	AGN Type
(1)	(2)	(3)	(4)	(5)	(6)	(7)	(8)	(9)	(10)	(11)	(12)	(13)
RX J1747.9+6538	2890	17 47 58.0	+65 38 35	17 47 57.9	+65 38 28	3.85	0.0305	0.0022	29.91	1.04	0.3248	1
RX J1748.2+7016	2900	17 48 17.4	+70 16 14	17 48 19.6	+70 16 09	3.93	0.0446	0.0036	44.20	0.43	0.1858	1
RX J1748.3+6403	2910	17 48 22.7	+64 03 27	17 48 23.1	+64 03 38	3.27	0.0155	0.0023	14.00	7.06	0.9859	1
RX J1748.6+6842	2940	17 48 38.8	+68 42 11	17 48 38.3	+68 42 17	4.25	0.0236	0.0023	24.28	0.02	0.0537	1
RX J1749.3+6411	3000	17 49 20.4	+64 11 08	17 49 19.5	+64 11 19	3.27	0.0109	0.0019	9.85	4.94	0.9836	1
RX J1749.7+6422	3001	17 49 42.4	+64 22 46	17 49 44.1	+64 22 58	3.24	0.0078	0.0017	7.02	1.83	0.7540	1
RX J1750.2+6814	3050	17 50 14.3	+68 14 33	17 50 16.1	+68 14 37	4.50	0.0069	0.0013	7.29	0.12	0.2310	1
RX J1750.2+6415	3060	17 50 15.5	+64 15 15	17 50 15.1	+64 14 56	3.11	0.0115	0.0019	10.13	0.19	0.2504	2
RX J1751.0+6710	3100	17 51 02.4	+67 10 09	17 51 01.2	+67 10 14	4.33	0.0038	0.0008	3.95	0.56	0.5870	1
RX J1751.1+6753	3120	17 51 09.5	+67 53 07	17 51 08.9	+67 53 08	4.45	0.0062	0.0011	6.52	0.25	0.3406	1
RX J1751.6+6540	3160	17 51 39.7	+65 40 40	17 51 36.9	+65 40 30	4.10	0.0122	0.0015	12.33	4.02	0.8259	1
RX J1751.9+6551	3190	17 51 57.6	+65 51 20	17 51 56.7	+65 51 17	4.13	0.0121	0.0012	12.28	0.65	0.3901	1
RX J1752.2+6624	3210	17 52 12.6	+66 24 56	17 52 11.7	+66 24 54	3.88	0.0049	0.0008	4.82	0.27	0.4002	1
RX J1752.9+6440	3230	17 52 57.4	+64 40 58	17 52 56.9	+64 40 56	3.22	0.0125	0.0016	11.21	0.04	0.1230	1
RX J1753.1+6746	40	17 53 09.7	+67 46 44	17 53 09.6	+67 46 32	4.77	0.0070	0.0011	7.60	5.37	1.1297	1
RX J1753.5+6811	3231	17 53 30.9	+68 11 47	17 53 32.4	+68 12 01	5.01	0.0056	0.0014	6.21	0.43	0.4366	2
RX J1753.6+6542	3260	17 53 41.6	+65 42 42	17 53 42.1	+65 42 40	4.34	0.0076	0.0009	7.90	0.04	0.1400	1
RX J1753.9+7016	3280	17 53 55.5	+70 16 47	17 53 56.6	+70 16 42	4.25	0.0095	0.0018	9.77	0.01	0.0620	1
RX J1754.0+6613	60	17 54 05.4	+66 13 54	17 54 04.8	+66 13 50	4.12	0.0152	0.0010	15.40	0.90	0.4067	1
RX J1754.7+6819	3340	17 54 42.3	+68 19 08	17 54 42.0	+68 19 06	5.23	0.0066	0.0011	7.46	0.27	0.3292	1
RX J1754.7+6208	3350	17 54 43.2	+62 08 21	17 54 42.3	+62 08 30	3.41	0.0147	0.0024	13.58	0.45	0.3190	1
RX J1754.8+6706	100	17 54 49.3	+67 06 00	17 54 49.7	+67 05 56	4.53	0.0023	0.0005	2.44	1.03	0.9190	1
RX J1755.0+6446	3360	17 55 00.0	+64 46 32	17 55 00.8	+64 46 32	3.49	0.0085	0.0013	7.94	1.65	0.6870	1
RX J1755.0+6235	3361	17 55 03.6	+62 35 30	17 55 03.2	+62 35 41	3.33	0.0083	0.0020	7.57	13.86	1.6607	1
RX J1755.0+6519	3370	17 55 05.8	+65 19 50	17 55 05.6	+65 19 55	3.78	0.0948	0.0030	92.17	0.14	0.0785	1
RX J1755.1+6719	110	17 55 09.0	+67 19 50	17 55 08.3	+67 19 54	4.69	0.0049	0.0008	5.28	0.08	0.2225	2
RX J1755.1+6852	3380	17 55 11.9	+68 52 30	17 55 10.7	+68 52 34	4.56	0.0062	0.0012	6.59	7.43	1.3645	1
RX J1755.6+6209	3420	17 55 40.3	+62 09 41	17 55 40.3	+62 09 39	3.41	0.0240	0.0027	22.17	0.04	0.0846	2
RX J1755.6+7009	3410	17 55 40.5	+70 09 52	17 55 41.3	+70 09 51	4.25	0.0077	0.0016	7.92	0.53	0.4295	1
RX J1755.7+6249	3430	17 55 46.2	+62 49 27	17 55 45.9	+62 49 29	3.33	0.0402	0.0034	36.67	0.61	0.2360	1
RX J1755.9+6540	140	17 55 56.9	+65 40 54	17 55 56.8	+65 40 52	4.15	0.0089	0.0009	9.05	0.31	0.3238	1
RX J1756.1+6615	160	17 56 10.0	+66 15 14	17 56 09.5	+66 15 09	4.01	0.0086	0.0007	8.60	1.48	0.6357	1
RX J1756.1+7001	3460	17 56 10.8	+70 01 55	17 56 11.9	+70 01 47	3.90	0.0090	0.0017	8.88	0.12	0.2129	1
RX J1756.1+7055	3470	17 56 10.8	+70 55 48	17 56 11.6	+70 55 50	4.25	0.0163	0.0022	16.76	0.31	0.2460	1
RX J1756.2+6619	170	17 56 12.0	+66 19 47	17 56 12.2	+66 19 46	4.01	0.0023	0.0004	2.30	1.64	1.1340	1
RX J1756.2+6955	3480	17 56 12.7	+69 55 21	17 56 12.7	+69 55 20	3.84	0.0177	0.0023	17.33	0.03	0.0838	2
RX J1756.2+6838	3490	17 56 13.6	+68 38 31	17 56 15.5	+68 38 25	5.24	0.0070	0.0012	7.92	0.02	0.1019	2
RX J1756.4+6300	3510	17 56 25.2	+63 00 42	17 56 25.4	+63 00 49	3.53	0.0077	0.0016	7.23	4.90	1.1110	1
RX J1756.7+6438	3530	17 56 43.2	+64 38 53	17 56 43.4	+64 38 59	3.49	0.0231	0.0019	21.57	0.32	0.2233	1
RX J1756.8+6612	180	17 56 52.4	+66 12 42	17 56 51.3	+66 12 42	4.14	0.0061	0.0006	6.20	7.78	1.4252	1
RX J1756.9+6238	3550	17 56 58.2	+62 38 44	17 57 00.6	+62 38 55	3.33	0.0205	0.0026	18.70	12.10	1.0902	1
RX J1757.1+6352	3570	17 57 09.7	+63 52 38	17 57 09.5	+63 52 33	3.31	0.0145	0.0019	13.19	0.45	0.3220	1
RX J1757.5+6841	3590	17 57 34.1	+68 41 22	17 57 34.1	+68 41 21	5.46	0.0205	0.0018	23.61	0.22	0.1814	1
RX J1757.9+6934	3600	17 57 55.2	+69 34 23	17 57 55.2	+69 34 25	4.35	0.0270	0.0024	28.09	0.04	0.0795	1
RX J1757.9+6609	210	17 57 56.9	+66 09 23	17 57 56.5	+66 09 20	4.26	0.0025	0.0005	2.58	0.23	0.4865	2
RX J1758.0+6851	3620	17 58 02.4	+68 51 46	17 58 03.7	+68 51 51	4.87	0.0061	0.0013	6.69	0.07	0.1876	1
RX J1758.2+7020	3621	17 58 12.4	+70 20 27	17 58 13.4	+70 20 23	4.25	0.0080	0.0018	8.23	5.94	1.1400	1
RX J1758.2+6743	230	17 58 13.2	+67 43 18	17 58 14.1	+67 43 17	5.02	0.0122	0.0012	13.55	0.16	0.2045	1
RX J1758.3+6906	3630	17 58 18.7	+69 06 30	17 58 15.9	+69 06 32	4.42	0.0104	0.0016	10.91	37.92	2.1572	1
RX J1758.3+6203	241	17 58 23.3	+62 03 26	17 58 24.4	+62 03 20	3.41	0.0078	0.0019	7.21	1.35	0.6590	1
RX J1758.4+6531	250	17 58 24.1	+65 31 05	17 58 24.2	+65 31 08	4.04	0.0195	0.0013	19.57	0.68	0.3250	1
RX J1758.7+6423	3680	17 58 44.5	+64 23 04	17 58 43.1	+64 23 04	3.38	0.0054	0.0011	4.97	1.29	0.7523	1
RX J1758.8+6551	280	17 58 52.8	+65 51 06	17 58 53.2	+65 51 13	4.40	0.0030	0.0005	3.14	0.17	0.3884	2
RX J1758.9+6220	3700	17 58 56.5	+62 20 31	17 58 56.3	+62 20 25	3.33	0.0070	0.0017	6.38	1.34	0.6910	1

TABLE 1 — *Continued*

Object	NEP ID	α_X (J2000)	δ_X (J2000)	α_{opt} (J2000)	δ_{opt} (J2000)	n_H [10^{20} cm^{-2}]	Count Rate [s^{-1}]	Count Rate Error [s^{-1}]	f_X [10^{-14} cgs]	L_X [10^{44} cgs]	z	AGN Type
(1)	(2)	(3)	(4)	(5)	(6)	(7)	(8)	(9)	(10)	(11)	(12)	(13)
RX J1759.3+6335	3730	17 59 19.2	+63 35 37	17 59 18.4	+63 35 40	3.15	0.0063	0.0014	5.59	4.92	1.2354	1
RX J1759.7+6739	350	17 59 42.5	+67 39 25	17 59 42.8	+67 39 27	5.35	0.0049	0.0007	5.60	3.56	1.0830	1
RX J1759.7+6629	360	17 59 44.3	+66 29 11	17 59 44.7	+66 29 11	4.12	0.0040	0.0004	4.06	0.23	0.3990	1
RX J1800.1+6636	380	18 00 07.5	+66 36 54	18 00 07.6	+66 36 55	4.17	0.0048	0.0004	4.89	0.001	0.0260	2
RX J1800.1+6938	381	18 00 08.4	+69 38 30	18 00 10.4	+69 38 38	4.56	0.0055	0.0013	5.85	3.57	1.0650	1
RX J1800.1+6720	390	18 00 11.2	+67 20 48	18 00 10.9	+67 20 58	4.68	0.0036	0.0006	3.87	2.82	1.1433	1
RX J1800.3+6615	430	18 00 23.1	+66 15 54	18 00 23.8	+66 15 52	4.03	0.0048	0.0005	4.81	0.35	0.4475	1
RX J1800.4+7051	3810	18 00 25.2	+70 51 55	18 00 25.8	+70 51 58	4.25	0.0101	0.0019	10.39	0.35	0.3200	1
RX J1800.4+6357	3820	18 00 26.2	+63 57 19	18 00 26.4	+63 57 19	2.72	0.0205	0.0020	16.83	3.44	0.6828	1
RX J1800.4+6705	440	18 00 29.0	+67 05 48	18 00 28.9	+67 05 50	4.52	0.0041	0.0005	4.34	4.62	1.3330	1
RX J1801.2+6433	3860	18 01 13.2	+64 33 22	18 01 14.7	+64 33 26	3.43	0.0061	0.0011	5.65	2.09	0.8700	1
RX J1801.2+6902	3870	18 01 14.6	+69 02 43	18 01 14.6	+69 02 43	4.86	0.0057	0.0012	6.24	5.89	1.2700	1
RX J1801.2+6624	480	18 01 15.2	+66 24 01	18 01 16.6	+66 24 01	4.05	0.0012	0.0002	1.21	1.09	1.2500	1
RX J1802.0+6629	560	18 02 05.9	+66 29 02	18 02 04.8	+66 29 14	4.14	0.0013	0.0003	1.32	0.03	0.2650	1
RX J1802.1+6535	570	18 02 07.7	+65 35 21	18 02 07.7	+65 35 14	4.23	0.0034	0.0007	3.49	0.02	0.1513	1
RX J1802.3+6259	3910	18 02 19.6	+62 59 21	18 02 21.5	+62 59 14	3.48	0.0063	0.0014	5.88	1.39	0.7240	1
RX J1802.3+6647	590	18 02 22.8	+66 47 49	18 02 24.5	+66 47 35	4.24	0.0047	0.0005	4.83	0.19	0.3424	1
RX J1802.7+6727	630	18 02 47.4	+67 27 50	18 02 47.8	+67 27 41	4.94	0.0026	0.0006	2.87	0.02	0.1620	2
RX J1802.8+6605	640	18 02 51.2	+66 05 40	18 02 51.3	+66 05 42	4.12	0.0166	0.0009	16.82	0.21	0.2070	1
RX J1803.4+6738	650	18 03 28.3	+67 38 06	18 03 29.0	+67 38 10	4.87	0.2801	0.0042	306.77	1.51	0.1360	1
RX J1803.8+6619	660	18 03 50.4	+66 19 31	18 03 50.1	+66 19 31	4.30	0.0064	0.0006	6.62	0.37	0.3968	1
RX J1804.5+6937	4020	18 04 34.2	+69 37 33	18 04 34.4	+69 37 37	4.76	0.0082	0.0016	8.90	1.36	0.6055	1
RX J1804.6+6846	4040	18 04 41.9	+68 46 02	18 04 40.6	+68 45 55	5.07	0.0072	0.0013	8.03	0.02	0.0969	2
RX J1805.2+7006	4080	18 05 16.6	+70 06 19	18 05 17.8	+70 06 22	4.19	0.0162	0.0024	16.55	0.16	0.1874	1
RX J1805.4+6638	710	18 05 25.3	+66 38 58	18 05 25.0	+66 39 03	4.10	0.0105	0.0008	10.61	0.06	0.1449	1
RX J1805.6+6624	720	18 05 36.1	+66 24 52	18 05 36.2	+66 24 52	4.10	0.0110	0.0008	11.12	2.60	0.7210	1
RX J1805.6+6309	4110	18 05 39.0	+63 09 36	18 05 40.1	+63 09 22	3.00	0.0080	0.0016	6.92	0.67	0.5013	1
RX J1805.6+6432	4120	18 05 41.4	+64 32 51	18 05 40.5	+64 32 47	3.35	0.0121	0.0015	11.07	2.78	0.7432	1
RX J1806.0+6940	4140	18 06 03.2	+69 40 26	18 06 03.2	+69 40 24	4.76	0.0087	0.0017	9.44	0.32	0.3214	1
RX J1806.2+6644	740	18 06 12.5	+66 44 40	18 06 12.4	+66 44 34	4.00	0.0041	0.0006	4.10	0.17	0.3482	1
RX J1807.7+6617	4270	18 07 47.4	+66 17 32	18 07 47.4	+66 17 31	3.94	0.0087	0.0008	8.63	3.82	0.9350	1
RX J1808.0+6452	4280	18 08 02.5	+64 52 24	18 08 03.7	+64 52 30	3.38	0.0211	0.0021	19.38	11.05	1.0360	1
RX J1808.8+6634	4390	18 08 49.8	+66 34 31	18 08 49.6	+66 34 29	3.85	0.0220	0.0013	21.59	4.64	0.6970	1
RX J1808.8+6530	4400	18 08 51.0	+65 30 21	18 08 50.8	+65 30 19	3.91	0.0095	0.0013	9.38	0.26	0.2937	2
RX J1808.8+6511	4401	18 08 53.4	+65 11 42	18 08 53.5	+65 11 48	3.82	0.0043	0.0010	4.20	7.40	1.6350	1
RX J1809.0+6704	4410	18 09 01.0	+67 04 21	18 09 00.9	+67 04 25	4.09	0.0046	0.0008	4.65	0.99	0.6950	1
RX J1809.0+6800	4420	18 09 03.5	+68 00 55	18 09 03.1	+68 00 57	4.47	0.0062	0.0012	6.53	0.95	0.5946	1
RX J1809.0+6333	4430	18 09 05.0	+63 33 00	18 09 05.5	+63 33 09	2.65	0.0073	0.0017	5.92	1.04	0.6412	1
RX J1809.5+6620	4440	18 09 30.1	+66 20 33	18 09 30.1	+66 20 21	3.86	0.0061	0.0009	5.99	1.03	0.6350	1
RX J1809.5+6609	4450	18 09 34.8	+66 09 06	18 09 34.2	+66 09 11	3.85	0.0055	0.0009	5.40	2.42	0.9400	1
RX J1809.7+6837	4460	18 09 46.8	+68 37 26	18 09 48.4	+68 37 34	5.36	0.0059	0.0012	6.74	0.09	0.2173	1
RX J1810.0+6344	4490	18 10 04.2	+63 44 24	18 10 04.4	+63 44 26	2.76	0.0223	0.0026	18.47	0.91	0.3770	1
RX J1810.3+6328	4501	18 10 23.5	+63 28 08	18 10 16.9	+63 29 14	2.74	0.0135	0.0025	11.12	3.76	0.8380	1
RX J1810.4+6432	4520	18 10 24.7	+64 32 46	18 10 24.2	+64 32 54	3.12	0.0067	0.0015	5.91	0.17	0.3030	1
RX J1811.2+6543	4550	18 11 12.4	+65 43 46	18 11 11.6	+65 43 47	3.94	0.0127	0.0014	12.59	1.15	0.4895	1
RX J1811.6+6507	4580	18 11 36.8	+65 07 04	18 11 36.1	+65 07 00	3.67	0.0197	0.0020	18.86	6.54	0.8470	1
RX J1811.6+6333	4590	18 11 41.2	+63 33 46	18 11 43.5	+63 33 51	2.72	0.0084	0.0019	6.90	0.25	0.3310	1
RX J1812.4+6610	4640	18 12 27.0	+66 10 46	18 12 26.1	+66 10 48	3.87	0.0036	0.0008	3.54	0.63	0.6449	1
RX J1813.0+6644	4670	18 13 04.8	+66 44 56	18 13 06.1	+66 44 52	4.56	0.0056	0.0010	5.96	1.62	0.7680	1
RX J1813.1+6547	4680	18 13 09.0	+65 47 01	18 13 07.7	+65 47 04	3.87	0.0102	0.0013	10.04	0.41	0.3489	1
RX J1813.1+6608	4690	18 13 10.7	+66 08 02	18 13 07.9	+66 08 09	3.83	0.0045	0.0009	4.40	4.75	1.3400	1
RX J1813.5+6635	4720	18 13 34.1	+66 35 36	18 13 35.1	+66 35 34	4.58	0.0038	0.0008	4.05	0.76	0.6609	1
RX J1813.6+6731	4721	18 13 41.5	+67 31 50	18 13 43.0	+67 32 23	4.67	0.0142	0.0019	15.27	2.44	0.6168	1
RX J1813.7+6538	4760	18 13 46.6	+65 38 21	18 13 45.8	+65 38 20	3.91	0.0342	0.0022	33.79	0.35	0.1912	1

TABLE 1 — *Continued*

Object	NEP ID	α_X (J2000)	δ_X (J2000)	α_{opt} (J2000)	δ_{opt} (J2000)	n_H [10^{20} cm^{-2}]	Count Rate [s^{-1}]	Count Rate Error [s^{-1}]	f_X [10^{-14} cgs]	L_X [10^{44} cgs]	z	AGN Type
(1)	(2)	(3)	(4)	(5)	(6)	(7)	(8)	(9)	(10)	(11)	(12)	(13)
RX J1813.8+6728	4800	18 13 51.0	+67 28 10	18 13 50.7	+67 28 06	4.63	0.0084	0.0015	9.00	0.30	0.3196	1
RX J1815.2+6658	4880	18 15 17.0	+66 58 10	18 15 17.4	+66 58 05	4.67	0.0070	0.0012	7.53	0.12	0.2287	2
RX J1815.3+6507	4890	18 15 19.1	+65 07 28	18 15 20.0	+65 07 14	3.85	0.0073	0.0015	7.16	14.36	1.7234	1
RX J1815.4+6806	4910	18 15 24.4	+68 06 29	18 15 24.9	+68 06 32	4.58	0.0214	0.0022	22.82	0.39	0.2390	1
RX J1815.8+6441	4930	18 15 52.3	+64 41 00	18 15 51.7	+64 41 03	3.16	0.0117	0.0020	10.38	0.63	0.4116	1
RX J1817.5+6631	5020	18 17 32.1	+66 31 08	18 17 31.3	+66 31 11	4.64	0.0083	0.0012	8.90	0.67	0.4513	1
RX J1818.4+6741	5050	18 18 28.9	+67 41 26	18 18 28.8	+67 41 24	4.64	0.1125	0.0044	120.64	3.87	0.3140	1
RX J1818.7+6518	5080	18 18 46.2	+65 18 14	18 18 44.8	+65 18 10	4.20	0.0056	0.0013	5.73	5.82	1.3080	1
RX J1819.8+6510	5150	18 19 52.2	+65 10 35	18 19 51.5	+65 10 37	4.21	0.0173	0.0020	17.72	0.18	0.1894	1
RX J1819.9+6628	5190	18 19 59.9	+66 28 25	18 19 59.0	+66 28 30	4.79	0.0049	0.0012	5.33	5.07	1.2740	1
RX J1820.5+6620	5230	18 20 32.9	+66 20 29	18 20 32.9	+66 20 20	4.71	0.0075	0.0015	8.09	0.80	0.5057	1
RX J1820.5+6930	5240	18 20 35.3	+69 30 04	18 20 33.4	+69 30 15	6.46	0.0160	0.0025	19.77	0.24	0.2051	1
RX J1821.6+6543	5300	18 21 38.8	+65 43 04	18 21 40.0	+65 43 10	4.26	0.0171	0.0020	17.63	0.39	0.2666	2
RX J1821.6+6328	5310	18 21 39.6	+63 28 27	18 21 38.8	+63 28 26	3.10	0.0282	0.0035	24.80	1.13	0.3656	1
RX J1821.9+6654	5321	18 21 55.7	+66 54 34	18 21 56.5	+66 54 26	5.07	0.0056	0.0011	6.24	0.01	0.0873	1
RX J1821.9+6420	5340	18 21 57.4	+64 20 51	18 21 57.1	+64 20 37	3.77	1.0710	0.0140	1039.63	29.32	0.2970	1
RX J1821.9+6818	5330	18 21 58.8	+68 18 42	18 21 59.4	+68 18 42	4.85	0.0073	0.0017	7.98	15.30	1.6920	1
RX J1823.3+6419	5400	18 23 20.0	+64 19 23	18 23 19.2	+64 19 32	3.32	0.0219	0.0026	19.95	2.70	0.5766	1
RX J1823.6+6847	5411	18 23 38.6	+68 47 40	18 23 39.4	+68 47 46	5.85	0.0085	0.0019	10.08	0.13	0.2071	1
RX J1823.9+6719	5440	18 23 54.6	+67 19 41	18 23 54.7	+67 19 36	4.75	0.0079	0.0015	8.56	0.65	0.4536	1
RX J1824.7+6509*	5500	18 24 46.9	+65 09 24	18 24 47.3	+65 09 25	3.97	0.1269	0.0048	126.39	3.73	0.3030	1
RX J1825.7+6905	5530	18 25 46.3	+69 05 51	18 25 47.3	+69 05 54	6.66	0.0362	0.0036	45.27	0.09	0.0888	1
RX J1826.6+6706	5550	18 26 38.3	+67 06 47	18 26 37.5	+67 06 44	5.48	0.0212	0.0023	24.46	0.64	0.2870	1
RX J1827.2+6549	5560	18 27 15.3	+65 49 21	18 27 13.9	+65 49 20	5.30	0.0071	0.0016	8.07	6.97	1.2250	1
RX J1827.5+6431	5590	18 27 33.6	+64 31 38	18 27 33.8	+64 31 44	4.16	0.0141	0.0022	14.35	0.03	0.0977	1
RX J1828.1+6709	5601	18 28 06.6	+67 09 23	18 28 06.7	+67 09 17	6.02	0.0085	0.0016	10.20	4.61	0.9430	1
RX J1828.2+6403	5620	18 28 13.7	+64 03 31	18 28 14.2	+64 03 28	3.83	0.0119	0.0023	11.64	0.03	0.0963	1
RX J1828.7+6953	5670	18 28 47.9	+69 53 58	18 28 49.3	+69 54 00	7.02	0.0271	0.0033	34.60	0.11	0.1100	1
RX J1828.8+6452	5680	18 28 48.6	+64 52 50	18 28 48.3	+64 53 00	4.42	0.0134	0.0020	14.05	5.25	0.8730	1
RX J1829.0+6433	5690	18 29 00.6	+64 33 49	18 29 00.4	+64 33 51	4.30	0.0183	0.0023	18.94	1.00	0.3880	1
RX J1829.5+6631	5740	18 29 35.4	+66 31 19	18 29 35.4	+66 31 23	6.21	0.0066	0.0016	8.03	1.68	0.6898	1
RX J1829.7+6749	5750	18 29 43.4	+67 49 09	18 29 42.2	+67 49 12	6.19	0.0158	0.0023	19.18	1.66	0.4783	1
RX J1830.0+6645	5790	18 30 01.4	+66 45 23	18 30 02.0	+66 45 23	6.38	0.0142	0.0021	17.45	0.46	0.2889	1
RX J1830.1+6425	5800	18 30 07.5	+64 25 28	18 30 06.1	+64 25 29	3.90	0.0104	0.0019	10.26	1.69	0.6253	1
RX J1832.0+6542	5890	18 32 01.5	+65 42 35	18 32 01.3	+65 42 33	5.41	0.0239	0.0026	27.42	0.74	0.2908	1
RX J1832.0+6447	5900	18 32 04.2	+64 47 01	18 32 01.2	+64 47 08	4.33	0.0177	0.0025	18.37	12.65	1.1180	1
RX J1832.4+6402	5930	18 32 25.2	+64 02 02	18 32 24.1	+64 02 10	4.93	0.0106	0.0022	11.68	0.59	0.3826	1
RX J1832.4+6438	5940	18 32 25.2	+64 38 15	18 32 24.2	+64 38 23	4.27	0.0140	0.0021	14.45	1.62	0.5335	1
RX J1833.0+6344	5990	18 33 02.8	+63 44 17	18 33 01.3	+63 44 35	4.93	0.0139	0.0024	15.31	1.88	0.5535	1
RX J1835.0+6526	6070	18 35 04.8	+65 26 44	18 35 06.0	+65 26 47	5.52	0.0206	0.0026	23.85	1.41	0.4083	1
RX J1835.1+6342	6080	18 35 08.0	+63 42 33	18 35 10.0	+63 43 14	4.93	0.0228	0.0033	25.12	11.40	0.9445	1
RX J1835.1+6733	6090	18 35 10.3	+67 33 54	18 35 09.0	+67 33 58	6.59	0.0075	0.0017	9.34	2.37	0.7460	1
RX J1836.4+6602	6180	18 36 28.2	+66 02 40	18 36 28.7	+66 02 37	7.08	0.0130	0.0024	16.65	0.16	0.1858	1
RX J1836.6+6719	6200	18 36 36.1	+67 19 04	18 36 36.8	+67 19 12	8.03	0.0084	0.0018	11.29	0.25	0.2693	1
RX J1838.1+6649	6280	18 38 09.1	+66 49 26	18 38 10.0	+66 49 22	7.17	0.0083	0.0019	10.69	0.28	0.2879	1
RX J1838.8+6432	6300	18 38 51.9	+64 32 21	18 38 53.1	+64 32 23	5.43	0.0081	0.0019	9.31	0.77	0.4700	1
RX J1839.2+6711	6301	18 39 16.9	+67 11 12	18 39 16.5	+67 11 06	8.24	0.0063	0.0015	8.55	1.94	0.7130	1
RX J1839.3+6544	6340	18 39 18.5	+65 44 42	18 39 18.3	+65 44 35	5.77	0.0095	0.0023	11.20	0.02	0.0820	1
RX J1841.3+6321	6450	18 41 18.9	+63 21 36	18 41 20.0	+63 21 42	5.32	0.0096	0.0022	10.94	15.55	1.4990	1
RX J1842.2+6204	6452	18 42 14.8	+62 04 24	18 42 15.6	+62 04 24	5.25	0.0146	0.0032	16.54	0.56	0.3203	1
RX J1842.5+6809	6490	18 42 33.0	+68 09 30	18 42 33.3	+68 09 25	6.35	0.0511	0.0044	62.70	5.33	0.4750	1
RX J1842.9+6241	6491	18 42 56.4	+62 41 44	18 42 55.2	+62 41 49	5.32	0.0502	0.0048	57.21	0.10	0.0835	1
RX J1843.3+6653	6520	18 43 22.5	+66 53 21	18 43 20.9	+66 53 29	7.33	0.0110	0.0022	14.28	0.50	0.3273	1
RX J1843.9+6821	6540	18 43 55.7	+68 21 11	18 43 54.1	+68 21 01	6.08	0.0200	0.0032	24.10	1.12	0.3688	1

TABLE 1 — *Continued*

Object	NEP ID	α_X (J2000)	δ_X (J2000)	α_{opt} (J2000)	δ_{opt} (J2000)	n_H [10^{20} cm^{-2}]	Count Rate [s^{-1}]	Count Rate Error [s^{-1}]	f_X [10^{-14} cgs]	L_X [10^{44} cgs]	z	AGN Type
(1)	(2)	(3)	(4)	(5)	(6)	(7)	(8)	(9)	(10)	(11)	(12)	(13)
RX J1844.3+6431	6542	18 44 23.4	+64 31 31	18 44 21.8	+64 31 46	6.00	0.0105	0.0022	12.59	1.13	0.4870	1
RX J1844.4+6236	6543	18 44 26.9	+62 36 12	18 44 26.4	+62 36 14	5.32	0.0274	0.0039	31.22	1.03	0.3172	1
RX J1844.4+6248	6544	18 44 27.5	+62 48 27	18 44 26.2	+62 48 29	5.32	0.0239	0.0034	27.24	67.62	1.8800	1
RX J1844.9+6813	6570	18 44 54.0	+68 13 23	18 44 54.1	+68 13 17	5.84	0.0250	0.0036	29.64	0.92	0.3097	1

* RX J1824.7+6509 (NEP 5500) was formerly classified as a stellar X-ray source based on the literature. However, more recent work convincingly demonstrates this source is a type 1 AGN at $z = 0.303$ (e.g., Engels et al. 1998).

NOTE — Table 1 is also available in machine-readable form in the electronic edition of the *Astrophysical Journal*.